

Magnetization and Anisotropy of Fe/Co (001) Multilayers:

A First-Principles Calculation

Marienette B. Morales

SUBMITTED IN PARTIAL FULFILLMENT  
OF THE REQUIREMENTS FOR THE DEGREE OF  
MASTER OF SCIENCE IN PHYSICS

AT THE  
UNIVERSITY OF THE PHILIPPINES

COLLEGE OF SCIENCE

NATIONAL INSTITUTE OF PHYSICS

DILIMAN, QUEZON CITY

March 2004

## CERTIFICATION

This is to certify that this graduate thesis entitled “ **Magnetization and Anisotropy of Fe/Co (001) Multilayers: A First-Principles Calculation** ” submitted by **Marienette B. Morales** in partial fulfillment of the requirements for the degree of **Master of Science in Physics**, was successfully presented, defended, and **approved** on March 2004.

CRISTINE VILLAGONZALO, DR. RER. NAT.  
Assistant Professor in Physics  
National Institute of Physics  
College of Science  
U.P. Diliman, Quezon City

RONALD BANZON, PH.D.  
Assistant Professor in Physics  
National Institute of Physics  
College of Science  
U.P. Diliman, Quezon City

MARISCIEL PALIMA, PH.D.  
Assistant Professor in Physics  
National Institute of Physics  
College of Science  
U.P. Diliman, Quezon City

The National Institute of Physics endorses acceptance of this graduate thesis as a partial fulfillment of the requirements for the degree of Master of Science in Physics.

CAESAR A. SALOMA, PH.D.  
Director  
National Institute of Physics  
College of Science  
U.P. Diliman, Quezon City

This graduate thesis is hereby officially accepted as partial fulfillment of the requirements for the degree of Master of Science in Physics.

RHODORA AZANZA, PH.D.  
Dean  
College of Science  
U.P. Diliman, Quezon City

# Table of Contents

List of Tables	vii
List of Figures	viii
Acknowledgements	x
List of Abbreviations	xii
Abstract	xiii
<b>1 Introduction</b>	<b>1</b>
<b>2 Properties of Magnetic Materials</b>	<b>8</b>
2.1 Magnetization and Magnetocrystalline Anisotropy . . . . .	8
2.2 Bulk Materials, Thin Films and Multilayers . . . . .	12
2.3 More Properties of Superlattices . . . . .	17
2.4 Fe/Co Superlattices . . . . .	19
<b>3 Numerical Method</b>	<b>20</b>
3.1 Theoretical Framework . . . . .	20
3.2 Exchange-Correlation Energy and Local Spin Density Approximation . . . . .	23
3.3 Computational Method . . . . .	26
3.4 Full-Potential Linear Muffin-Tin Orbital Method (FP-LMTO) . . . . .	27
3.5 Implementation of Electronic Structure Calculation . . . . .	32

3.5.1	Self-Consistency Method . . . . .	32
3.5.2	Computational Details . . . . .	34
3.6	Magnetic Moment and Magnetic Anisotropy Energy Calculation . . . . .	36
<b>4</b>	<b>Results</b>	<b>38</b>
4.1	Equilibrium Parameters for Bulk Fe and Co . . . . .	39
4.2	Fe/Co Multilayers . . . . .	48
4.2.1	Equilibrium Energy . . . . .	49
4.2.2	Magnetocrystalline Anisotropy . . . . .	50
4.2.3	Magnetization . . . . .	51
4.2.4	Intermixing . . . . .	57
<b>5</b>	<b>Summary and Conclusions</b>	<b>62</b>
<b>A</b>	<b>Magnetovolume Sensitivity of Fe and Co Multilayers</b>	<b>65</b>
	<b>Bibliography</b>	<b>69</b>

# List of Tables

1.1	Selected Breakthroughs in Multilayers Studies . . . . .	4
4.1	FPLMTO calculations of the magnetic moment per atom and magnetic anisotropy energy per atom of bcc Fe and bcc Co in bulk. . . . .	48
4.2	Difference in equilibrium energy per atom of multilayers with respect to bulk Fe and Co. . . . .	50
4.3	FPLMTO calculations of the magnetic moment per atom and magnetic anisotropy energy per atom of Fe <sub>7</sub> /Co <sub>1</sub> , Fe <sub>6</sub> /Co <sub>2</sub> , Fe <sub>5</sub> /Co <sub>3</sub> , Fe <sub>4</sub> /Co <sub>4</sub> and Fe <sub>1</sub> Co <sub>7</sub> . The total energies were calculated for superlattice spin at [001], [100] and [110] axes. Note that the easy axis of all the multilayers is the [110] direction. . . . .	51
4.4	Difference in equilibrium energy per atom of Fe <sub>6</sub> /Co <sub>2</sub> multilayer with intermixed Fe and Co layer compared to bulk Fe and Co and Case 1. . . . .	57

# List of Figures

1.1	Number of publications on metallic and magnetic multilayers gathered from Institute of Electrical Engineering (IEE)-INSPEC database [28]. The data only include publications up to year 1999. . . . .	3
2.1	Relative positions of electron cloud (ellipsoid) and spin direction (arrow) of neighboring atoms in a lattice. Rotations in spin orientation causes magnetic anisotropy. The energy of (a) is in general different from (b). . . . .	10
2.2	Orientation of magnetization, $M$ , relative to the $[010]$ crystal axis in the presence of magnetic field, $H$ . . . . .	12
2.3	Crystal axes direction in a cubic atom such as Fe and Ni. . . . .	13
3.1	Schematic diagram of muffin-tin spheres. Light spheres are the top layer and dark spheres belong to the next layer as viewed from the $[001]$ direction. . . . .	28
3.2	Flow Diagram for Self-Consistent Field Density Functional-Based Method for Electronic Structure Calculation . . . . .	33
4.1	Position of the eight atoms in the supercell stacked along $[001]$ axis. The in-plane and out-of-plane lattice constant is 5.20 Bohr ( $2.71 \text{ \AA}$ ). Also shown are the different crystal lattice directions. . . . .	40
4.2	Geometry of the supercells: (a)Fe <sub>7</sub> /Co <sub>1</sub> , (b)Fe <sub>6</sub> /Co <sub>2</sub> and (c)Fe <sub>5</sub> /Co <sub>3</sub> . Dark-colored spheres are Fe atoms and the light-colored ones are Co atoms. . . . .	41
4.3	Geometry of other supercells: Dark-colored spheres are Fe atoms and the light-colored ones are Co atoms. (a)Fe <sub>4</sub> /Co <sub>4</sub> and (b)Fe <sub>1</sub> /Co <sub>7</sub> . . .	42
4.4	Changes in total energy of Fe bulk as a function of the total number of $k$ points in the whole Brillouin zone. $E_o$ is the most accurate energy computed with higher BZ density. . . . .	45

4.5	Bulk bcc iron. This shows the ground state energy and volume of magnetic bulk iron. Total energy differences are normalized with respect to the lowest energy, $E_{min}$ , obtained in magnetic Fe. . . . .	46
4.6	Bulk bcc cobalt. This shows ground state energy and lattice volume of hypothetical magnetic bulk bcc cobalt. Total energy differences are normalized with respect to the lowest energy, $E_{min}$ , obtained in magnetic Co. . . . .	47
4.7	Calculated MAE per volume as a function of Co concentration. . . . .	52
4.8	Calculated average spin moments of Fe/Co multilayers, Fe <sub>7</sub> /Co <sub>1</sub> , Fe <sub>6</sub> /Co <sub>2</sub> , Fe <sub>5</sub> /Co <sub>3</sub> , Fe <sub>4</sub> /Co <sub>4</sub> , Fe <sub>1</sub> /Co <sub>7</sub> for different Co concentrations. Solid line represents Fe bulk moment and dashed line marks the Co bulk moment. . . . .	54
4.9	Calculated spin moments of atom at the interface of Fe/Co multilayers, Fe <sub>7</sub> /Co <sub>1</sub> , Fe <sub>6</sub> /Co <sub>2</sub> , Fe <sub>5</sub> /Co <sub>3</sub> , Fe <sub>4</sub> /Co <sub>4</sub> , Fe <sub>1</sub> /Co <sub>7</sub> for increasing Co concentrations. Solid line represents Fe bulk moment and dashed line marks the Co bulk moment. . . . .	55
4.10	Calculated spin moment of atoms close to the interface of Fe/Co multilayers, Fe <sub>7</sub> /Co <sub>1</sub> , Fe <sub>6</sub> /Co <sub>2</sub> , Fe <sub>5</sub> /Co <sub>3</sub> , Fe <sub>4</sub> /Co <sub>4</sub> , Fe <sub>1</sub> Co <sub>7</sub> for different Co concentrations. Solid line represents Fe bulk moment and dashed line marks the Co bulk moment. . . . .	56
4.11	Fe <sub>6</sub> /Co <sub>2</sub> multilayers. The layers composed of Co atoms are intermixed with Fe layers. Case 1: adjacent Co atoms; Case 2: 2 monolayers of Fe separate the 2 Co layers. Case 3: 1 monolayer thickness apart. . . . .	58
4.12	Calculated magnetic moment of atoms in the Fe <sub>6</sub> /Co <sub>2</sub> multilayer for the 3 different cases. Solid line represents Fe bulk moment and dashed line marks the Co bulk moment. Region inside the box contain magnetic moments of Co atoms and the remaining in the graph are magnetic moments of Fe atoms. . . . .	60
4.13	Intermixed portions of Fe <sub>6</sub> /Co <sub>2</sub> multilayer in Cases 2 and 3 configurations. The increase in magnetic moment of the sandwiched Fe layer in (a) is 27% while in (b) is 17% compared to the bulk Fe moment. . . . .	61
A.1	Magnetic moment of bulk bcc Fe and bcc Co as a function of lattice volume. . . . .	66
A.2	Layer by layer magnetic moment of Fe/Co multilayers calculated using Fe and Co lattice constants . . . . .	67

# Acknowledgements

This work is possible only because of the dedicated supervision of my adviser, **Dr. Cristine Villagonzalo**. Indeed, the things I learned while working with her on this project go beyond what is found in this written work. For her generosity and patience, I express my great appreciation.

The draft of the manuscript was read by **Dr. Ronald Banzon** and was critiqued by the rest of my panel members, **Dr. Marisciel Palima** and **Dr. Roy Tumlos**. I am grateful to their valuable suggestions.

My masters study was funded by the Department of Science and Technology - Philippine Council for Advanced Science and Technology Research and Development (**DOST-PCASTRD**). Also, a research grant was received from the Creative and Research Scholarship of the **OVPAA - University of the Philippines**. To the members of these councils, I extend my gratitude.

I sincerely thank **Marites L. Violanda**, for all the meaningful conversations.

But for her encouragement and support, this work would not have been undertaken.

For keeping the computing machines and networks up and running, many thanks are also due to the National Institute of Physics' and Structure and Dynamics group's systems administrators, **Johnrob Bantang** and **Melvin Estonactoc**.

To my Ateneo de Manila colleagues, whose names are worth mentioning: **Yoli, Joel, Ma'am Libay, Paeng, Michelle, Adrian and Reese**, thank you for always lending an ear during my most trying times. Special thanks to **Clint Bennett**, Physics department's systems administrator. You are all part of my success.

My parents, **Ernesto and Nenita Morales**, have worked as hard in the completion of this endeavor in my life. Their dedication to me and confidence in me has never wavered all these years. For all the love and more, I express my deepest gratitude and appreciation. To my sister, **Joann**, who continues to be my reality check in all things at all times, thank you.

My sincerest thanks are due to the one person that truly inspires me and gives special meaning to all my hard work, **Michael Francis Ian Vega**, who despite the distance has never failed to give me strength and make me feel loved.

Finally, I owe everything and offer everything to the most generous **Lord, Almighty**.

*With much love and gratitude, I dedicate this work to God, my parents and Ian.*

# List of Abbreviations

BCC	body-centered cubic
BZ	Brillouin zone
FCC	face-centered cubic
FP-LMTO	full-potential linear muffin tin orbital method
GMR	giant magnetoresistance
HCP	hexagonal closed-pack
IEC	interlayer exchange coupling
LMTO	linear muffin-tin orbital method
MAE	magnetic/magnetocrystalline anisotropy
MT	muffin-tin
SCF	self-consistent field
IFC	Intel Fortran Compiler

# Abstract

Magnetic properties of bcc Fe/Co (001) multilayers have been successfully calculated from first-principles. The computational framework of this study is based on the FP-LMTO (full-potential linear muffin tin orbital) method within the density functional theory.

The ground state configuration of the the bulk bcc Fe has been reproduced including the correct easy axis of [100]. For a hypothetical bcc Co in bulk, the easy axis was suggested to be at [001] direction. Calculated magnetic moments of the bulk materials are  $2.05 \mu_B$  and  $1.72 \mu_B$  for Fe and Co, respectively. Total energy method was implemented to resolve MAE (magnetic anisotropy energy) as low as 0.89 nRy involving spin directions at [001] and [100] for Fe while giving a value of  $7.06 \times 10^{-6}$  nRy for Co. Results are compared with the accepted theoretical values as well as with available experimental results and are found to be in good agreement.

MAE and magnetization of the multilayers are extensively investigated for different concentrations of Fe and Co. Calculations were done for bcc Fe<sub>7</sub>/Co<sub>1</sub>, Fe<sub>6</sub>/Co<sub>2</sub>, Fe<sub>5</sub>/Co<sub>3</sub>, Fe<sub>4</sub>/Co<sub>4</sub> and Fe<sub>1</sub>/Co<sub>7</sub>. All the multilayer systems have easy axis along [110] axis. We have also provided detailed magnetic profiles of the atoms in the multilayers. For Fe/Co multilayers, magnetic moment of Fe atoms located at the interface is enhanced by 24% compared to the magnetic moment of pure Fe in bulk. It is also higher by 10% compared to the magnetic moments of other Fe atoms found in the multilayer, especially if located farther from the interface. The greatest enhancement in magnetic moment is observed for the multilayer with  $\sim 88\%$  Co content. Average moments are found to decrease as the multilayer becomes richer in Co. MAE also increases for increasing Co concentrations and/or layer thickness.

The intermixing in the Fe and Co layers that occur in atomically unsharp interfaces of multilayer was also modelled. Even more dramatic increase in magnetic moments was observed when there is only one monolayer thickness of impure interface, i.e., having one monolayer of Fe sandwiched between two Co layers. Ground state energy calculations also determine the stability of the multilayers in various configurations.

# Chapter 1

## Introduction

Development of new materials has been the focus of modern condensed matter and materials physics research in the recent years. The study of these new materials, particularly magnetic ones, are very important as it provides the underlying science for several technological applications. Several of these materials are made by layering two or more types of metals or alloys alternately on top of one another to form a superlattice or multilayer. Superlattice was the term originally used to refer to multilayer structures larger than one bilayer in thickness that exhibit correlated properties along the growth direction. However, the two terms have been frequently used interchangeably. The smallest unique sequence in superlattice, which is being repeated along the growth axis is called the supercell.

Stimulated by rapid advances in technologies for synthesis of materials and techniques for characterization, more and more superlattices have been grown in various configurations. These techniques allow epitaxial growth of thin films a few atomic monolayers thick in stacks to form a highly crystalline material. Deposition is achieved with low contamination, minimal surface defects and clear-cut interfaces because the technique can be flow-rate controlled. Ultra high vacuum (UHV) molecular beam epitaxy (MBE) and DC sputtering [17, 18, 42] are being used more frequently compared to pulsed laser deposition (PLD) [24, 48] and ion beam sputtering (IBS) [11, 13]. UHV MBE, which makes use of atom beams to deposit films on a substrate at considerably high temperature, has the unique advantage that it can be coupled with surface characterization tools such as reflection high energy electron diffraction (RHEED) [38] and Auger electron spectroscopy (AES) [27].

Although metallic multilayers have been studied for more than six decades now [19], it was only in the 1980s that researchers have successfully used magnetic metals in multilayers. Significant impact of multilayers in magnetism research became evident in 1990s as seen in Figure 1.1 the tremendous increase in number of publications on this field. Table 1.1 features selected achievements in multilayers, highlighting the relevant studies for magnetism.

Magnetic multilayers show a variety of unusual magnetic behaviors when compared to bulk materials, mostly attributed to interface effects, including scattering

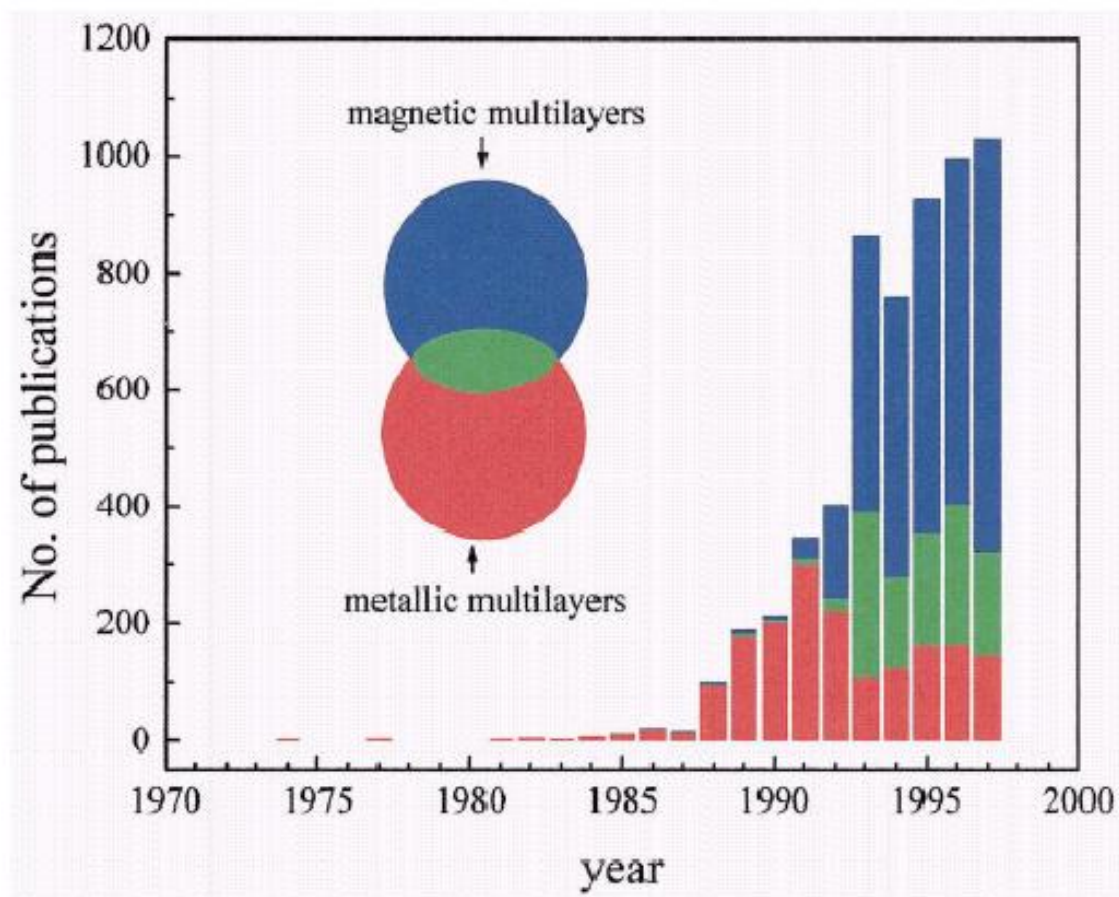


Figure 1.1: Number of publications on metallic and magnetic multilayers gathered from Institute of Electrical Engineering (IEE)-INSPEC database [28]. The data only include publications up to year 1999.

Table 1.1: Selected Breakthroughs in Multilayers Studies

Year		Ref.
1935	Fabrication of metallic superlattices and multilayers	[19]
1978	Anomalous magnetization in Cu/Ni	[53]
1980	Lattice mismatched superlattices	[47]
1982	Absence of 2D magnetism in Cu/Ni	[25]
1986	Antiferromagnetic coupling in Fe/Cr sandwiches	[22]
1988	Giant magnetoresistance in Fe/Cr (GMR)	[3]
1989	Growth of bcc Co thin films	[29]
1991	Perpendicular transport in multilayers	[44]
1992	Local magnetic moments in bcc Co	[36]
1995	Fabrication of Co/Ni using sputtering technique	[20]
1998	Magnetic phases of Fe in Fe/Ni	[34]
2002	Growth and magnetic anisotropy of bcc Fe/Co superlattice	[40]

at the interface, spin polarization and magnetic interactions. Although it is believed that interface magnetism contributes to this, the nature of its exact origin is unclear. In fact, these are central issues on the study of transition metals over the last few years. A lot of work has been devoted to this subject largely due to the technological possibilities provided by these new materials.

One of the most important properties of magnetic materials is the magnetocrystalline or magnetic anisotropy. Magnetic anisotropy is the intrinsic persistence of ferromagnets to an easy direction of magnetization. Different degrees of magnetic anisotropy is desired in different applications, such as permanent magnets, information storage devices and recording/read heads. Therefore, it is important to study the effect of atomic position, structure, temperature and composition on the anisotropy

of a material.

Magnetic properties depend on the structural properties of the multilayers [59, 60]. A basic design of a multilayer crystal consists of a double layer of ferromagnetic metal separated by a nonmagnetic metal. In the presence of small external fields, the two ferromagnetic layers align themselves parallel or anti-parallel with respect to each other. This is brought about by the spin dependent Coulomb interaction of charges or interlayer exchange coupling (IEC). IEC has been, both experimentally [9, 22] and theoretically [10], shown to depend on the thickness of the magnetic layers. This particular arrangement of metals also exhibit giant magnetoresistance (GMR) effect [3, 4, 9, 40]. GMR effect is the dramatic change of electrical resistivity through the nonmagnetic layer. The drop in resistivity has been found to depend on the change in the relative magnetic orientation of the ferromagnetic layers to one another. Apparently, the two phenomena involve, though not confined to, the spin redirection of the ferromagnetic layers. The required energy to change the magnetization direction is the magnetic anisotropy energy (MAE). MAE critically depends on temperature, thickness and composition [2, 9, 40]. The structure also affects the behavior of the saturation magnetization or magnetization value at low fields. This is observed to change, generally increases, for most materials. Enhancement in the magnetic moment is observed at the interface. It is believed that this is due to the mutual disturbance between the two materials in the interface region. Hence, the positions and type

of atoms in the superlattice are deterministic factors of the magnetic properties. In experiments, layer resolved magnetic moments are difficult to measure. Information on the magnetic moment of atoms with overlayers may be experimentally measured using magnetic circular x-ray dichroism but very few have done it [51, 54].

As seen in most literature, magnetic superlattices composed of ferromagnetic/non-magnetic (F/N) materials attracted more attention than those composed of ferromagnetic/ferromagnetic (F/F) or ferromagnetic/rare-earth materials. In the present work, the magnetic properties of an alternative multilayer system consisting of two ferromagnetic materials having different degrees of magnetization, namely iron and cobalt, are investigated. We will look into the detailed magnetic profile of the interface between Fe and Co, relating it to their corresponding bulk properties. Cobalt naturally occurs in the hexagonal close-packed structure (hcp). But grown on a body-centered cubic (bcc) Fe, Co may take a bcc structure. Very little is known about bcc cobalt, which can be stabilized in thin films but not in bulk. Co grown with a bcc structure is particularly interesting to study since it is a material rarely used as a spacer layer. Fe/Co properties have been verified in experiments but few offer theoretical support.

In this paper, we will perform first-principles calculations to determine numerically the magnetic moment and MAE of bcc Fe/Co multilayer. A highly-precise numerical method, which is the full potential-linear muffin tin orbital (FP-LMTO) method [58]

is used and numerical results are compared with experimental and other theoretical results where available. Other researchers have done full-potential calculations on noble metal/Co bilayers [45] while others have worked on pseudopotential calculations on metal alloys [46]. To our knowledge, so far very few full-potential calculations have been performed for the chosen multilayer materials to explain the experimentally observed large MAE. The numerical technique also made it possible to calculate layer resolved spin moments to give a vivid description of the magnetic properties of Fe/Co superlattices.

The rest of the paper is organized as follows: The next section, Chapter 2, discusses the fundamental concept of magnetism in bulk materials, thin films and multilayers. We also review in this chapter the recent experimental and theoretical results in the study of magnetic materials, which lead to the novel and practical applications. Chapter 3 discusses the theoretical foundations of the density-functional based numerical method used, which is FP-LMTO. The structure of the chosen model system and details of the numerical implementation is also found in this chapter. Chapter 4 discusses the results of the numerical calculations. We will see that magnetic moments of Fe atoms located the interface of an Fe/Co multilayer is greatly increased compared to that of a bcc Fe found in bulk. Other energetically stable configurations involving this new material will also be described in this chapter. Lastly, summary and recommendations are presented in Chapter 5.

# Chapter 2

## Properties of Magnetic Materials

### 2.1 Magnetization and Magnetocrystalline

#### Anisotropy

Magnetization occurs when magnetic moments of atoms align in a regular manner. In most materials, the magnetic moments separated into several magnetic domains, are oriented randomly when there is no magnetic field applied. When a magnetic field is present, the magnetic moments arrange themselves parallel or antiparallel with respect to other domains. Different materials have varying degree of magnetic ordering in the presence of a magnetic field. However, there are certain elements, which exhibit spontaneous magnetic moments or appearance of aligned magnetic moments in the absence of an applied field. These are called ferromagnetic materials.

Examples of ferromagnetic metals are Fe, Co and Ni.

The mechanism responsible for ferromagnetism is attributed to Pauli' exclusion principle, which inhibits two electrons of similar spins to occupy the same orbital. The magnetization value is defined by magnetic moment per unit volume. Every unpaired electron contributes 1 Bohr magneton ( $\mu_B$ ) to the total magnetic moment of the atom. In bulk, Fe has a magnetic moment of  $2.2 \mu_B$  whereas Co has  $1.7 \mu_B$  [32].

The magnetization generally lies in some preferred directions with respect to the crystalline axes called the easy axis. This property is known as the magnetocrystalline anisotropy. It is due to the electron distribution of atoms in a lattice being asymmetric. A schematic diagram of this distribution is shown in Figure 2.1. It is like an ellipsoid rather than perfectly spherical and this asymmetry provides a mechanism for magnetic anisotropy. Since the electron cloud is fixed with the orientation of the magnetic moment, any changes in spin direction relative to the crystal axes changes the energy. The energy involved in rotating the magnetization to another direction, as well as the direction of the easy axis of a magnetic material can be described by the magnetocrystalline anisotropy energy (MAE). This is defined to be the difference in total energies of the same system but with different magnetization directions, i.e., the easy and hard axes.

For cubic and uniaxial crystals, the MAE is expressed in the series expansion in

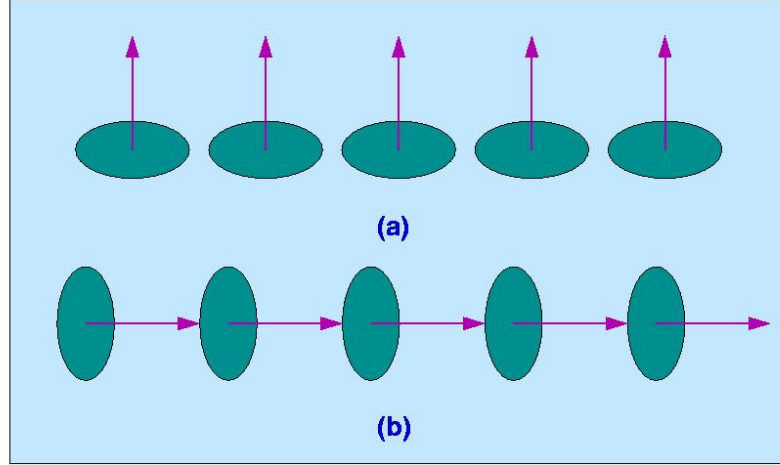


Figure 2.1: Relative positions of electron cloud (ellipsoid) and spin direction (arrow) of neighboring atoms in a lattice. Rotations in spin orientation causes magnetic anisotropy. The energy of (a) is in general different from (b).

terms of the direction cosines, which is the angle between the direction of magnetization and the lattice axes.

$$E_{a,cubic} = K_1(\alpha_1^2\alpha_2^2 + \alpha_2^2\alpha_3^2 + \alpha_3^2\alpha_1^2) + K_2(\alpha_1^2\alpha_2^2\alpha_3^2 + \dots) \quad (2.1)$$

where  $\alpha_i$  are the direction cosines and  $K_1$  and  $K_2$  are the first and second order anisotropy constants, respectively. The anisotropy constants are separated into interface and volume contributions  $K_i = K_{i,Volume} + 2K_{i,Surface}/d$ ,  $i = 1, 2, 3, \dots$ . For uniaxial crystals, the MAE is in the form of

$$E_{a,uniaxial} = K_1\sin^2\theta + K_2\sin^4\theta + \dots \quad (2.2)$$

where  $\theta$  is the angle of magnetization with respect to the stacking direction of the lattice. It is usually sufficient to represent the anisotropy energy in an arbitrary

direction using only the first two terms in the series expansion[45].

In the presence of an external field, the MAE is obtained by analyzing the magnetization curve measured along a hard axis [8]. The energy due to the applied field is given by the Zeemann term expressed as

$$E_H = -\mu_o \vec{M}_s \cdot \vec{H} . \quad (2.3)$$

The magnetic field is denoted by  $\vec{H}$ ,  $\vec{M}_s$  is the magnetization and  $\mu_o$  is the magnetic permeability. The energy required to rotate the magnetization is

$$E_H = E_a - \mu_o H M_s \cos(\theta_o - \theta) , \quad (2.4)$$

where  $E_a$  is the energy when there is no applied field,  $\theta_o$  is the angle between the easy axis and the applied field whereas  $\theta$  is the angle between the easy axis and the saturation magnetization. In Figure 2.2, consider a material with easy axis along [010] direction. When anisotropic fields (H), are present, the magnetization ( $M_s$ ) becomes noncolinear with the easy axis. The magnetic anisotropy energy is obtained by minimizing (2.4) with respect to  $\theta$ .

The MAE may be obtained experimentally from direct magnetization measurements using superconducting quantum interference device (SQUID) magnetometer [8, 37, 40]. It can also be obtained theoretically by implementing force-theorem [2, 50, 56], and total energy calculation [45, 55].

Typically, MAE of ferromagnetic materials is in the order of  $10^{-6}$  to  $10^{-3}$  eV/atom [55]. In Fe, the easy direction is the [100] direction, the [110] is the intermediate and

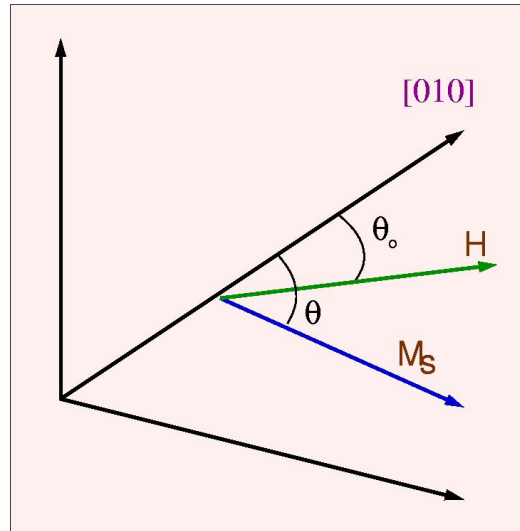


Figure 2.2: Orientation of magnetization,  $M$ , relative to the  $[010]$  crystal axis in the presence of magnetic field,  $H$ .

the  $[111]$  is the hard axis. In Ni,  $[111]$  and  $[100]$  are the easy and hard directions, respectively [32]. For reference, the crystal axes of a cubic atom is shown in Figure 2.3.

## 2.2 Bulk Materials, Thin Films and Multilayers

Magnetic properties of materials in bulk are different from those of corresponding sample in thin films. There is a decrease in the number of nearest neighbors of an element in thin films since spatial dimensions has been reduced. In general, this leads to changes in magnetic properties. For 3d transition metals, the spin magnetic

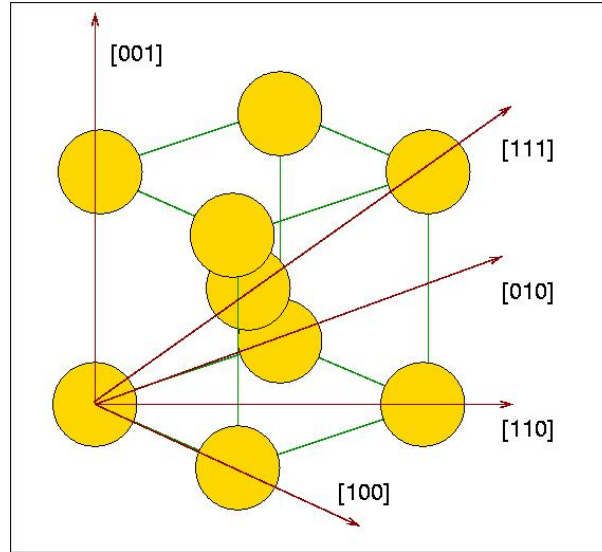


Figure 2.3: Crystal axes direction in a cubic atom such as Fe and Ni.

moment is generally enhanced. Although, this depends on the metal onto which it is grown. For example, there is an increase of Fe moment to  $2.5 \mu_B$  for a monolayer of Fe adjacent to Au [21]. Moments of magnetic thin films, therefore, are expected to increase. In fact, very thin films of vanadium (V) and palladium (Pd), which are naturally non-magnetic, can be made to be ferromagnetic because of this.

In recent years, magnetic properties, particularly the MAE of 3d transition metals in thin films, have been the subject of several theoretical investigations [12, 15, 16, 45, 52, 55, 60], usually in comparison with that of the corresponding bulk form of constituents atoms and alloys. In these studies, they calculated the MAE of free-standing thin films of metals and pure metallic films layered with noble metals. The magnetization of free-standing Co as well as Co-based multilayers, such as Co/Pd,

Co/Au and Co/Ag is oriented perpendicular to the plane for sufficiently thin Co layer. Thus, based on this property, these elements are potential candidates for high-density storage media. The accepted theory to explain this phenomenon, as suggested in earlier work [14], is that the magnetization couples with the lattice through spin-orbit interaction. However, the mechanism responsible for this phenomenon is not fully understood. Moreover, these material do not exhibit a high degree of magnetic anisotropy. In fact, the MAE give a very small value and its measurement and calculation would require resolving energies in the order of  $60 \mu\text{eV}/\text{atom}$  for uniaxial hcp Co and even 50 times smaller for cubic Fe and Ni. Previous calculations used an approach that imposed geometrical constraint on the charge density and potential through the atomic-sphere approximation (ASA). Of all the multilayers considered in the work of Daalderop et al, the largest anisotropy is observed for hcp Co/Pd<sub>2</sub> attributed to the strain Co layer induced by the mismatch between Co and Pd. This verifies the prediction of a perpendicular magnetic anisotropy on Co-based thin film multilayers. There have been developments since the previous work to address the technical problems in resolving extremely small differences in energy. Total energy calculations are based on full-potential method, which can be modified to treat the MAE problem [55]. This was done for bcc Fe, fcc Co and fcc Ni with spins polarized along [001] and [111], hcp Co with [0001] and [10 $\bar{1}$ 0] spin polarization. The MAE was found to be smaller than  $0.05 \mu\text{eV}$  for all samples. The experimental easy axes are

correctly reproduced for Fe, face-centered cubic (fcc) Co and hcp Co, which are [001], [111] and [0001], respectively. However, the method did not identify the correct easy axis of [111] for fcc Ni. Another first-principles calculations have been performed on a magnetic FeCo alloy film, of varying concentrations, on a Cu(001) substrate [59]. The self-consistent calculations were carried out by using a spin-polarized, scalar relativistic version of screened Korringa-Kohn-Rostoker (KKR) method. They found that magnetic moments are oriented out-of plane for an alloy thickness of two monolayer and that above four monolayers, only in-plane magnetization is present.

Materials can now be tailored as intricately as possible with the development and improvement of depositing techniques. Metallic atoms cannot only be made into thin films, it can also be layered on top of or sandwiched between different materials. Being able to tailor materials to a specific design and subject these to suitable conditions become very important aspects as magnetic properties critically depend on structure, such as the number and distances of nearest neighbors as well as environmental conditions, such as temperature. In a recent experimental work, Fe is layered with vanadium (V) through UHV sputtering. The easy axis becomes more and more out of plane with decreasing magnetic Fe thickness. Moreover, hybridization and alloying of Fe and V produce an enhancement in the MAE. The saturation magnetization of this particular superlattice is found to be reduced compared to bulk iron and it favors [110] as easy direction [2].

Another remarkable process that can be achieved with the new synthesis techniques is the growth of unusual structures. Atoms can be forced to grow and form thin films having metastable states, a phase completely unknown in bulk. This can be done by choosing an appropriate substrate with matching lattice parameters. The 3d metals Fe, Co and Ni naturally has a surface structure of bcc, hcp and fcc, respectively. Co can be made to exist as fcc if grown on Cu and a bcc Co can be grown on GaAs (110) and also on Fe. Recently, the team of Nordblad, et. al, [40] has successfully deposited thin bcc Co films on Fe and reported on the interesting properties of this unique structure. There is an inversion in the sign of MAE as the system becomes richer in Co. With this design, the magnetic moment significantly increased compared to that of FeCo bulk alloy [40].

Magnetocrystalline anisotropy and magnetization materials in thin films are expected to change since the symmetry of atoms changed. We can investigate on this by analyzing the anisotropy energy of a uniaxial single crystal. Usually, it is sufficient to consider only the lowest order term of the energy [8],

$$E_a = K \sin^2 \theta , \quad (2.5)$$

where  $K$  is the effective anisotropy constant and  $\theta$  is the angle between the magnetization and the normal surface. We can express  $K$  as

$$K = \frac{2K_{surface}}{d} + K_{volume} - \mu_o M^2 . \quad (2.6)$$

The first term is the ratio of the anisotropy contribution from the two surfaces (hence,

the factor 2) of the film and the film thickness,  $d$ . The second term accounts for the volume anisotropy brought about by lattice mismatching. The last term denotes the shape anisotropy, which diminishes in the presence of interface roughness.

In bulk, the first term of (2.6) significantly diminishes due to increasing number of atomic layers such that the second term dominates and the magnetization tend to lie in the plane. However, in thin films and layers, it is the first term that dominates and for stability, the magnetization prefer to be perpendicular to the plane [7]. This phenomenon of perpendicular anisotropy finds promising applications in high-density information storage [21].

## 2.3 More Properties of Superlattices

The superlattice made by alternating ferromagnetic layer with a nonmagnetic spacer layer exhibit other interesting properties. It is possible for the ferromagnetic layers to interact across the spacer layer, even though it is nonmagnetic, through spin-dependent scattering called interlayer exchange coupling (IEC). The magnetic moments of ferromagnetic layers can align themselves either parallel or anti-parallel with respect to each other. IEC has been found to oscillate from ferromagnetic (parallel) or antiferromagnetic (anti-parallel) with respect to spacer layer thickness. The magnitude also changes rapidly with increasing spacer layer thickness. The phenomenon can be attributed to quantum interference due to confinement in the non-magnetic

layer [10].

The expression for IEC between two ferromagnetic layers, A and B, is given by [30]

$$J_{AB} = \frac{\mu_o M_s H_{sat} t_{fm}}{4}, \quad (2.7)$$

where  $\mu_o$  is the magnetic permeability,  $M_s$  is the saturation magnetization,  $H_{sat}$  is the saturation field and  $t_{fm}$  is the ferromagnetic layer thickness.

Of great interest due to its applications is the giant magnetoresistance (GMR), which is closely associated to IEC phenomenon. Initially antiferromagnetically aligned multilayers can exhibit large changes in electrical resistance as a current is passed along the plane of the layers. The current causes the moments to rotate and couple ferromagnetically. This is due to the reduction of scattered particles at this particular alignment. It was previously observed in Fe/Cr superlattice, which shows GMR effects as high as 50 – 60% when magnetic fields higher than  $20kOe$  are applied. As with all other phenomenon on magnetic materials, GMR is affected by layer thickness. It has been reported that Fe/V superlattices exhibit GMR effects when antiferromagnetic coupling is largest [9].

With these observations, IEC was then concluded as precedent for GMR effect. However, soon after, it was found that the effect can still be observed with uncoupled structures [21]. The only precondition for GMR is a rotation in the direction of magnetizations of succeeding ferromagnetic films.

## 2.4 Fe/Co Superlattices

Superlattices consisting of Fe and Co are very useful because it allows investigation of Co in a bcc structure. In earlier literature, it has been shown that bcc bulk alloys have [111] as the easy axis [14, 36], and thus exhibit perpendicular magnetic anisotropy (PMA), which from a technology point of view, is a desirable feature. But that is not the case for Fe/Co multilayers. A recent study investigates on the direction of the hyperfine field of atomic layers of Fe close to the bcc Co layer [35] and found that there is no evidence of an out-of-plane component of magnetic moment for Fe with magnetic moments confined in-plane along [110].

In a recent paper by Eriksson, et. al. [41], the computed average spin moment using real space-linear muffin tin orbital method in the atomic-sphere approximation (RS-LMTO-ASA) method was shown to decrease with increasing Co concentration but increasing initially such that the average spin moment is highest when the system of bcc Fe/Co multilayers consist of 25% Co. The same trend was observed when full-potential-LMTO was implemented. There is also an enhancement of the magnetic moment of Fe as large as  $2.6\mu_B$ . They were able to identify the easy axis of Fe to be along [100] and found that there is a transition of easy axis from [100] to [110] for 40 – 50% Co. Calculated MAE for the  $\text{Fe}_{1-x}/\text{Co}_x$  ( $x=2-12$ ) systems ranges from 0.7 to  $-0.5 \mu\text{eV}/\text{atom}$ .

# Chapter 3

## Numerical Method

### 3.1 Theoretical Framework

Most of the properties of solids can be traced to the arrangement and behavior of the electrons that make up the solid. One way to theoretically study these properties is by using first-principles calculations, which is done by implementing fundamental quantum theory and finding a solution to the time-independent Schrödinger equation.

$$H\Psi = E\Psi . \tag{3.1}$$

While analytic as well as exact numerical solutions of the Schrödinger equation can be found for systems with small number of atoms, it is very difficult to obtain the same for systems involving large numbers of atoms in the order of  $10^{23}$ . We wish to discuss the magnetic properties of metallic solids, hence, it is necessary to consider

a many-particle problem. We go about this problem by first expressing the suitable Hamiltonian of the system.

One of the most widely used schemes for first-principles or '*ab initio*' calculations is that based on the density functional theory (DFT). The central theme of DFT is that it is possible and advantageous to shift the dependence on the external potential to the dependence on the charge density distribution [43]. Here only the atomic number and lattice parameters of constituent atoms are employed as main input data.

The two theorems of Hohenberg and Kohn provide the basis for the calculations of the ground-state properties of an n-particle system in an external potential,  $V_{ext}$ . According to these theorems, the total energy can be written as a functional of the charge density  $\rho(\vec{r})$ ,

$$E[\rho] = \int V_{ext} \rho(\vec{r}) d^3r + F[\rho] , \quad (3.2)$$

where  $F[\rho]$  is the Hohenberg and Kohn free energy and is a functional of  $\rho(\vec{r})$ . The charge density which minimizes  $E[\rho]$  gives the true ground-state density. An explicit expression for  $F[\rho]$  is made up of the sum of the kinetic energy of non-interacting electrons,  $T_o$ , the Coulomb potential,  $V_C$ , and the energy of the remaining interactions denoted by  $E_{XC}$  or exchange-correlation energy. In symbols,

$$F[\rho] = T_o + V_C + E_{XC} . \quad (3.3)$$

The Thomas-Fermi method provide an approximate solution to this equation by calculating the non-interacting and interacting energies separately [31]. This method

has been found to give a rough description of the Coulomb potential and the charge density distribution as it did not include the contribution from  $E_{XC}$ . Initial attempts to consider  $E_{XC}$  did not give the correct results. The total energy calculation was greatly improved by Kohn and Sham when they introduced a different separation of the terms in the equation [1]. The energy functional in (3.2) can be rewritten as

$$E[\rho] = T_o[\rho] + \int \rho(\vec{r}) [V_{ext} + V_C] d^3r + E_{XC}[\rho] . \quad (3.4)$$

Given only the charge density, the first term is exactly evaluated by finding the corresponding effective potential,  $V_{eff}$  and using the single-particle Schrödinger equation,

$$[\nabla^2 + V_{eff}] \psi_i(\vec{r}) = \epsilon_i \psi_i(\vec{r}) . \quad (3.5)$$

The effective potential is obtained by taking the functional derivative of the last three terms of (3.4), such that

$$V_{eff}(\vec{r}) = V_{ext}(\vec{r}) + V_C(\vec{r}) + \frac{\delta E_{XC}[\rho]}{\delta \rho} . \quad (3.6)$$

This is the potential energy which the non-interacting electrons need to have in order to reproduce the density of interacting electrons. Here, the first and second terms are readily obtained as  $V_{ext}(\vec{r})$  is known and the Coulomb potential is determined by

$$V_C = \int d^3r' \frac{2 \rho(r')}{r - r'} . \quad (3.7)$$

Given a practical approximation of  $E_{XC}$ , this fully defines  $V_{eff}(\vec{r})$ . Substituting

$V_{eff}(\vec{r})$  back into (3.5), we are able to determine  $\psi_i$ , which in turn determines

$$\rho(\vec{r}) = \sum_{i=1}^N |\psi_i|^2 , \quad (3.8)$$

where  $N$  is the known number of electrons.

The equations above are the Kohn-Sham equations and are to be solved self-consistently until a converged  $V_{eff}$  or  $\rho(\vec{r})$  is obtained. In other words,  $V_{eff}$  determines  $\rho$  using (3.5) and is determined by it in (3.6).

## 3.2 Exchange-Correlation Energy and Local Spin Density Approximation

As we have seen, all the terms in (3.6) can readily be obtained from empirical input, except for  $E_{XC}$ . We have noted that the exchange-correlation energy describes all other interactions not included in the  $V_{ext}$  and the Coulomb interaction. Thus,  $E_{XC}$  is defined as the difference between the exact energy and other contributions that can be obtained numerically [1, 31]. Here, we need to apply some approximations on  $E_{XC}$ . By employing the local density approximation (LDA), where it is assumed that the electron density is slowly varying, we get

$$E_{XC}[\rho] = \int \rho(\vec{r}) \epsilon_{XC}[\rho] d^3r , \quad (3.9)$$

where  $\epsilon_{XC}$  is the exchange correlation energy per electron and depends only on  $\rho(\vec{r})$ .

The exchange correlation potential is easily obtained from this

$$V_{XC}(\vec{r}) = \frac{d}{d\rho}[\rho(\vec{r}) \epsilon_{XC}[\rho]] . \quad (3.10)$$

A refinement on the accuracy of LDA, which is implemented for spin polarized systems is the local-spin density approximation (LSDA) [26]. This takes into account that  $E_{XC}$  of spin-up and spin-down electrons are entirely different. Hence separate densities,  $\rho_{\uparrow}$  and  $\rho_{\downarrow}$ , are used. Therefore, exchange-correlation energy and potential are also allowed to be spin-dependent.

In the LSDA, Eq. 3.9 is expressed as

$$E_{XC}^{LSDA}[\rho_{\uparrow}, \rho_{\downarrow}] = \int \rho(\vec{r}) \epsilon_{XC}[\rho_{\uparrow}, \rho_{\downarrow}] d\vec{r} \quad (3.11)$$

where  $\rho(\vec{r}) = \rho_{\uparrow} + \rho_{\downarrow}$ . The explicit form of  $\epsilon_{XC}$  is expressed in terms of the fundamental standard variables  $r_s$  and  $\zeta$  for density and polarization, respectively.

The polarization  $\zeta$  is determined by using

$$\zeta = \frac{\rho_{\uparrow} - \rho_{\downarrow}}{\rho} .$$

We employ the well-known expression for the exchange energy,  $E_X$  according to the work of Vosko et al [57],

$$\epsilon_X(r_s, \zeta) = \epsilon_X^P(r_s) + [\epsilon_X^F(r_s) - \epsilon_X^P(r_s)]f(\zeta) . \quad (3.12)$$

where P and F denotes the paramagnetic and ferromagnetic states, respectively. Also with,

$$\begin{aligned}\epsilon_X^P(r_s) &= \frac{\epsilon_X^F(r_s)}{2^{1/3}} \\ \epsilon_X^P(r_s) &= \frac{-3}{2\pi\alpha r_s}\end{aligned}$$

and

$$\alpha = \left(\frac{4}{9\pi}\right)^{1/3}.$$

The function  $f(\zeta)$  has the form

$$f(\zeta) = \frac{[(1 + \zeta)^{4/3} + (1 - \zeta)^{4/3} - 2]}{2(2^{1/3} - 1)}. \quad (3.13)$$

There is no simple closed form for the correlation energy,  $\epsilon_C$ , but it may be written in the same form as the exchange energy in Eq. 3.12

$$\epsilon_C(r_s, \zeta) = \epsilon_C^P(r_s) + [\epsilon_C^F(r_s) - \epsilon_C^P(r_s)]f(\zeta), \quad (3.14)$$

where  $\epsilon_C^P(r_s) = \epsilon_C(r_s, 0)$ . The correlation contribution  $\epsilon_C = \epsilon - \epsilon_H - \epsilon_X$  is found to be substantial for all values of  $r_s$  and  $\zeta$  [23].  $\epsilon$  is the exact energy and the Hartree energy,  $\epsilon_H$ , is written in the form of

$$\epsilon_H = \frac{3}{10\alpha^2 r_s^2} [(1 + \zeta)^{5/3} + (1 - \zeta)^{5/3}].$$

The expression for the exchange-correlation energy (per particle) can be generalized in the formula

$$\epsilon_{XC}(r_s, \zeta) = \epsilon_{XC}^P(r_s) + [\epsilon_{XC}^F(r_s) - \epsilon_{XC}^P(r_s)]f(\zeta), \quad (3.15)$$

where

$$f(\zeta) = \frac{[(1 + \zeta)^{4/3} + (1 - \zeta)^{4/3} - 2]}{(2^{4/3} - 2)}$$

and

$$\begin{aligned} \epsilon_{XC}^i(r_s) = & \epsilon_X^i(r_s) - c^i[(1 + x_i^3)\ln(1 + 1/x_i) \\ & + 1/2x_i - x_i^2 - 1/3], \quad i = P, F, \end{aligned}$$

with  $x_i = r_s/r_i$  and  $c^i$ s are fractional constants. The values of these parameters were already accurately determined in previous work [23].

### 3.3 Computational Method

With the use of the effective potential, the Hamiltonian of the system has been reduced to that of a one-particle system, as in (3.5). Next we need to calculate the parameters that enter into the Hamiltonian from first principles relating them to the linear muffin-tin orbital (LMTO) electronic calculations [50].

With an initial external potential,  $V_{ext}$ , the initial charge density is obtained from

$$\rho(\vec{r}) = \sum_{j=1} |\psi_j|^2 . \quad (3.16)$$

The new effective potential can be calculated by adding the result of Poisson's equation, given by

$$\nabla^2 V_C(\vec{r})_i = -4\pi \sum_{j=1, j \neq i} |\psi_j|^2 , \quad (3.17)$$

and the exchange correlation potential. A converged  $V_{eff}$  or  $\rho(\vec{r})$  is obtained through self-consistency process. We can say that convergence has been met when the difference in the input and output potential is only a very small value,  $\delta$ , which is set arbitrarily small. As a technique to achieve convergence, it is usually necessary to utilize the combination of both the old and new solution to substitute to equation (3.5). This step is called the mixing process [50]. Using this potential, we can calculate the parameters using a tetrahedral mesh of suitable  $\mathbf{k}$ -points to perform the integration over the Brillouin zone.

The total energy of the system can be now be evaluated. In this step, we make use of the Born-Oppenheimer approximation that assumes the electron are faster-moving than the nuclei [50]. The density is therefore also dependent on the position of the nuclei and spin of the electrons. By uniqueness theorem, we are assured that the potential that solves the total energy equation is the true potential to within a constant.

### **3.4 Full-Potential Linear Muffin-Tin Orbital Method (FP-LMTO)**

In the full-potential linear muffin-tin orbital method calculations, no approximation is made on the shape of the density or potential. Their expansion is such that it no

longer requires spherical symmetry. Another strength of this method is that it allows unlimited basis functions to be assigned to each atom in the unit cell.

To solve the Hamiltonian, we need to form the sets of basis functions in which the wavefunctions are expanded. The linear muffin-tin orbital (LMTO) method provides the useful basis functions by dividing space into non-overlapping muffin-tin spheres centered at each atomic positions and an interstitial region between the muffin-tin spheres. The MT radii of the two kinds of atoms are chosen such that MTs fill most of the lattice space without overlapping one another as in Figure 3.1.

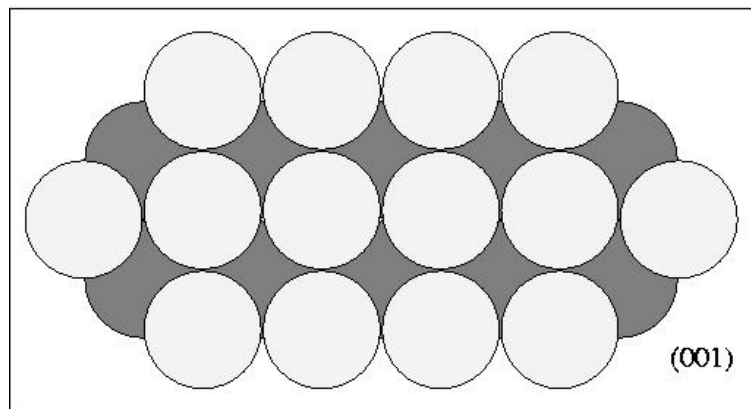


Figure 3.1: Schematic diagram of muffin-tin spheres. Light spheres are the top layer and dark spheres belong to the next layer as viewed from the  $[001]$  direction.

The radius of the MT sphere is centered at  $\tau$ . In the MT sphere, the potential,  $V_{MT}(\mathbf{r})$ , is spherically symmetric while in the interstitial, the potential,  $V_o$ , is constant. The two potentials initially need not be continuous at the MT boundary. The lattice positions are denoted by vectors  $\mathbf{R} = \mathbf{Rn}$ , integer multiples of a basis  $\mathbf{R}$ .

In the interstitial region,  $I$ , basis sets are Bloch sums of spherical Hankel or Neumann functions:

$$\psi_i(\mathbf{k}, \mathbf{r}) = \sum_R \exp i(\mathbf{k} \cdot R) K_l(\kappa_i, |\mathbf{r} - \tau_i - R|) Y_{lm}(D_\tau(\mathbf{r} - \tau_i - R)) , \quad (3.18)$$

where  $K_l$  indicates the Bessel functions given by

$$K_l(\kappa, r = -\kappa^{l+1}) \begin{cases} n_l(\kappa, r) - ij_l(\kappa, r) , & \kappa^2 < 0 \\ n_l(\kappa, r) , & \kappa^2 > 0 \end{cases} \quad (3.19)$$

The orbital moment quantum number is denoted by  $l$  and  $n_l$  and  $j_l$  are the spherical Neumann and Bessel functions, respectively. The kinetic energy,  $\kappa^2$  is the tail parameter that dictates the behavior of the orbital at the interstitial region. In the MT sphere, basis sets are linear combinations of spherical waves that matches continuously to the interstitial basis set in Eq. 3.18. At the parent MT site,  $\mathbf{R} = 0$  is compactly expressed using

$$K_l(\kappa, r) = (K_l(\kappa, r), J_l(\kappa, r)) \quad (3.20)$$

and the vector  $\mathbf{S}$  given by

$$S_{L,L} = \left\{ \begin{array}{c} \delta(\tau, \tau')\delta(L, L') \\ B_{L,L}(\kappa, \tau - \tau', k) \end{array} \right\}. \quad (3.21)$$

Note that  $L=(lm)$  and  $B$  is equivalent to the KKR (Korringa-Kohn-Rostoker) structure constant [33].  $J_l$  is the Bessel function,

$$J_l(\kappa, r) = \frac{j_l(\kappa r)}{\kappa^l} . \quad (3.22)$$

At the MT boundary, the basis function is expressed as

$$\psi_i(\mathbf{k}, r)|_{r_\tau=s_\tau} = \sum_L Y_L(D_\tau \hat{\mathbf{r}}) K_L(\kappa_i, s_\tau) S_{L,L'}(\kappa, \tau - \tau', k) . \quad (3.23)$$

The wavefunctions in the muffin tins sites, therefore, are expanded by means of spherical harmonic functions, indexed by  $h$ , multiplied by the radial component. The radial component is the linear combination of the functions  $\phi$  and their energy derivative  $\dot{\phi}$ .

The dependence of the MT basis set for every symmetry type,  $t$ , with the cut-off angular momentum parameter,  $l_m$  is explicitly seen in the expression

$$\psi_i(\mathbf{k}, r)|_{r_\tau < s_\tau} = \sum_L^{l \leq l_m} U_{tL}(e_i, D_\tau \hat{\mathbf{r}}) \Omega_{tL}(e_i, \kappa_i)(\kappa_i, s_\tau) S_{L,L'}(\kappa, \tau - \tau', k) , \quad (3.24)$$

where  $e_i$  is the energy parameter corresponding to the principal quantum number and

$$U_{tL}(e, \mathbf{r}) = Y_L(\hat{\mathbf{r}}) U_{tL}(e, r) . \quad (3.25)$$

In most cases, the angular momentum cut-off used ranges from  $l_m = 6$  to 8 for a converged total energy to be achieved. Taking the value  $l_m = 6$  is usually sufficient.

Once we have determined the basis sets in the three different parts: interstitial, inside the MT sphere and the MT boundary, we can now construct the matrix elements.

In the MT, the potential is expanded in the form of

$$V(\mathbf{r})|_{r_\tau < s_\tau} = \sum_h v_{ht}(r_\tau) D_{ht}(D_\tau \hat{\mathbf{r}}) \quad (3.26)$$

$$\text{where} \quad D_{ht}(\hat{\mathbf{r}}) = \sum_m \alpha_{ht}(m) \mathbf{C}_{l_h m}(\hat{\mathbf{r}}) . \quad (3.27)$$

The expression above contains the following spherical harmonics:

$$Y_{lm}(\hat{\mathbf{r}}) = i^l Y_{lm}(\hat{\mathbf{r}}) \quad (3.28)$$

$$C_{lm}(\hat{\mathbf{r}}) = \sqrt{\frac{4\pi}{2l+1}} Y_{lm}(\hat{\mathbf{r}}) \quad (3.29)$$

$$\mathbf{C}_{lm}(\hat{\mathbf{r}}) = i^l C_{lm}(\hat{\mathbf{r}}) . \quad (3.30)$$

Combining Eqs. 3.24 and 3.27, the potential matrix is obtained by  $\langle |\psi_i|V|\psi_j\rangle|_{MT}$ .

The interstitial overlap matrix is obtained by solving  $\langle |\psi_i|\psi_j\rangle|_I$  and the interstitial potential,  $V_{\mathbf{r}}$ , has rapidly converging Fourier coefficients:

$$V_{\mathbf{r}} = \sum_S \tilde{V}(S) D_S(r) \quad (3.31)$$

$$\text{where } D_S = \sum_{\mathbf{g} \in S} \exp i(\mathbf{g} \cdot \mathbf{r}) . \quad (3.32)$$

Note that FPLMTO method only provides the suitable expansion for the bases in the different regions. The charge density and the potential are obtained self-consistently. In each self-consistent loop, the basis functions are used determine the wave functions, which will be used in constructing the new charge density and potential. Having calculated the set of eigenvalues and eigenvectors from the eigenvalue problem, we can now obtain the charge density in the interstitial region given by

$$\tilde{\rho}(\mathbf{r})|_I = \sum_S \tilde{\rho}(S) D_S(\mathbf{r}) . \quad (3.33)$$

The Coulomb potential in this region is expressed as

$$V_C(\mathbf{r})|_I = \sum_{\mathbf{g} \neq 0} \frac{4\pi e^2 (\tilde{\rho}(\mathbf{g}) + \rho^{(p)}(\mathbf{g}))}{g^2} \exp i(\mathbf{g} \cdot \mathbf{r}) , \quad (3.34)$$

where  $\rho^{(p)}$  include the Fourier components. The Coulomb potential in the interstitial region has the same form as the Coulomb potential on the surface of the MT sphere. Inside the MT sphere, on the other hand, is given by

$$V^C(\mathbf{r})|_{r_\tau < s_\tau} = \sum_h D_{ht} \left[ e^2 \int_0^{s_\tau} \frac{r^{l_h} <}{r^{l_h+1} >} \frac{4\pi r'^2 \rho_h(r)}{2l_h + 1} dr' \right. \\ \left. + (V_h^{(C)} - \frac{e^2}{s^{l_h+1}} \int_0^s \frac{4\pi r'^{l_h+2} \rho_h(r')}{2l_h + 1} dr') \left(\frac{r}{s}\right)^{l_h} \right], \quad (3.35)$$

where  $V_{ht}^{(C)}$  is the harmonic component of the potential on a sphere boundary.

## 3.5 Implementation of Electronic

### Structure Calculation

#### 3.5.1 Self-Consistency Method

Figure 3.2 shows the flow diagram for calculating electronic structures. The method implemented is a self-consistent field method based (SCF) on the density-functional theory. The primary step is to identify a system of atoms and choose the structure. These information can be patterned from known fundamental concepts. Moreover, earlier experimental results normally provide these.

For SCF method, the basis functions need to be specified. Then the frozen-core approximation is employed for simplification of calculations. With a given initial potential, the Hamiltonian,  $H$ , and overlap functions,  $O$ , can already be formulated.

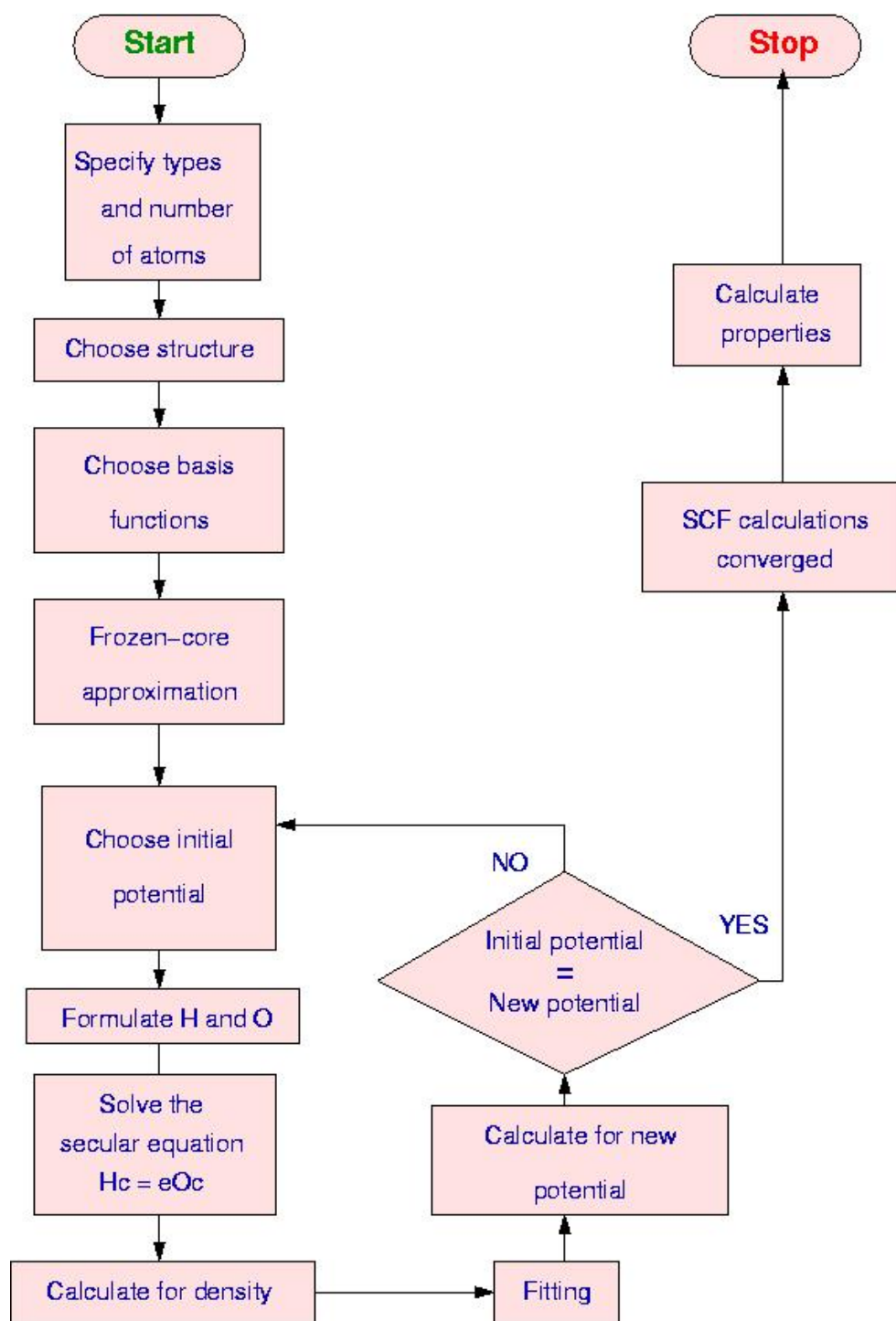


Figure 3.2: Flow Diagram for Self-Consistent Field Density Functional-Based Method for Electronic Structure Calculation

This gives rise to the secular equation,

$$[H - \epsilon(k) O] u = 0$$

where  $\mathbf{u}$  is a column vector containing the coefficients  $c_i$  and the energy eigenvalue  $\epsilon$  must be solved for each wave vector (k-point) $\mathbf{k}$ . The density,  $\rho$  is calculated. This new density is used to obtain a new potential. The process of setting up the secular equation from  $H$  and  $O$  is repeated until convergence is achieved. Once the new potential differs from the initial potential only by a very small value, properties such as total energy and spin moment of the system are calculated.

### 3.5.2 Computational Details

All the calculations in this work were carried out using the Intel Fortran compiler (IFC), which requires a Linux operating system. The machine used operates on a Pentium 4 processor. Computations for a non-spin polarized bulk system using a single atom in a supercell typically require about 3000 iterations taking 3-5 minutes each iteration depending on the temperature or starting potential used before convergence is achieved. Compared with non-spin polarized systems, spin-polarized total energy calculations for the same system of atoms is slower due to doubling in the size of the Hamiltonian matrix. Convergence is sought initially for lower BZ density and changing the BZ density to a higher value 150  $k$  points increases the computing time per iteration to around 13 minutes. The number of iteration in this case can be lower

even if the BZ density is larger since a more converged value for potential and energy parameter will be utilized. If a well-converged set of potential and energy parameter are used, the number of iterations can decrease to only about 120.

When there are more atoms comprising the supercell, such as in the multilayer case, more number of iterations are done and the time it takes to finish a single iteration is longer. Calculation time also varies with the number of layers in the supercell. For the same number of atoms that are arranged to form a wider supercell but with fewer number of layers, the required number of iterations are relatively lower than when they form taller supercells. Time per iteration, though is more or less the same for the two cases. On the average, for a system of a spin-polarized eight-atom supercell, which form 8 layers in thickness normally require 5000 iterations to reach convergence in both the total energies and spin moments. For this configuration, each iteration takes 45 minutes to 1 hour. No generalization, however, can be made as to whether the type of atoms and/or structure of the supercell (whether cubic or closed-pack) affect the time of convergence. For selected supercells, although identical atoms were used, run time can even be longer compared to that composed of two types of atoms. Another important detail to note is that when the lattice constant is changed, oftentimes, only require a single run of 60 iterations is required provided a well-converged potential is used. However, when spin polarization direction is changed, more iterations are needed. In obtaining the converged ground state configuration of

a particular magnetic multilayer system, the average number of iterations can reach up to 7000, taking  $\sim 1$  hour each time.

In the present work, we used the Fortran code for FP-MLTO originally developed by the late David Price of the University of Memphis. Initially designed to output the total spin moment of the system, the code was modified so that it can solve for the layer by layer magnetic moment of the superlattice by employing additional steps. It can now distinguish the contributions of the individual muffin-tins to the net spin moment from that obtained at the interstitial region. Note that the energy values are expressed in units of milliRydbergs (mRy), where  $1 \text{ mRy} = 13.6 \text{ meV}$ , and lengths are measured in units of bohr ( $1 \text{ Bohr} = 0.529 \text{ \AA}$ ).

## 3.6 Magnetic Moment and Magnetic Anisotropy

### Energy Calculation

The magnetic moment,  $m(\mathbf{r})$  is solely a function of the charge density and is calculated from the expression

$$m(\mathbf{r}) = -\mu_B(\rho_{\uparrow}(\mathbf{r}) - \rho_{\downarrow}(\mathbf{r})) \quad (3.36)$$

where  $\mu_B$  is the Bohr magneton equivalent to  $\mu_B = e\hbar/2m_e$ .

The total energy obtained from the calculation described in the previous section is used in computing for the MAE. It requires resolving the difference in total energies

when the magnetization is pointing in two different directions [15].

In this work, we make use of the total energy method for theoretical determination of MAE. With this technique, the spin configuration which gives the minimum total energy is the easy axis. The total energy is then calculated for other arbitrary spin directions and the difference between the total energies of the two cases gives the MAE. This amount of energy, therefore, is required to rotate the magnetization from a direction of lowest energy toward a hard axis of highest energy.

The anisotropy energy arises mainly from the detailed electronic structure, thus it is important to specify a large number of  $\mathbf{k}$  points to obtain a more accurate results in the integration over the BZ. However, compared with nonspin-polarized total energy calculation, calculations for spin-polarized system becomes a lot slower due to doubling in the size of the Hamiltonian matrix and reduction in the crystal symmetry.

# Chapter 4

## Results

Equilibrium parameters for bulk Fe and Co were initially determined for bulk bcc Fe and Co. Energy minimization method has been rigorously performed to qualify the choice of Brillouin zone (BZ) density, multiple *kappa* ( $\kappa$ ) set, muffin-tin (MT) radius and equilibrium lattice volume. Results obtained in this step were used when constructing the multilayers.

The supercell is composed of eight atoms, which are stacked successively in the direction of the [001] axis. This forms 4 cubic stacks of a bcc conventional cell with eight monolayers where one monolayer is the single center-to-center distance between adjacent x-y plane atoms. When a bilayer A/B is considered, it is formed by depositing atom B on top of A. Figure. 4.1 shows the positions of the atoms in a single supercell and the diagram of the superlattices being considered in this paper,

namely  $\text{Fe}_7/\text{Co}_1$ ,  $\text{Fe}_6/\text{Co}_2$ ,  $\text{Fe}_5/\text{Co}_3$ ,  $\text{Fe}_4/\text{Co}_4$  and  $\text{Fe}_1/\text{Co}_7$  multilayers having perfect interfaces are shown in Figures 4.2 and 4.3. In the figures, a top layer made of Fe is placed to show that since the computational method used assumes periodic boundary conditions, the layer adjacent to the topmost Co layer of the eight-atom supercell is once again an Fe layer.

All atomic sites in the lattice are occupied by a constituent atom, i. e., no empty sphere sites were used to indicate a semi-infinite boundary. The supercell region being considered is sufficiently far from the buffer and capping layers, hence, no surface effects are investigated. Moreover, no relaxation forces are considered in the computations and thus the resulting multilayers maintain a bcc structure with a fixed lattice constant.

## 4.1 Equilibrium Parameters for Bulk Fe and Co

In solving for the MAE, one of the problems one faces is the sampling of the BZ. Since anisotropic energy are typically very small, it is important to have a fine mesh of  $k$  points to obtain accurate results. The choice of BZ density is crucial in this kind of self-consistent calculation and that the total energy needs to be converged first with respect to the number of  $k$  points. To illustrate this we show in Figure 4.4 the

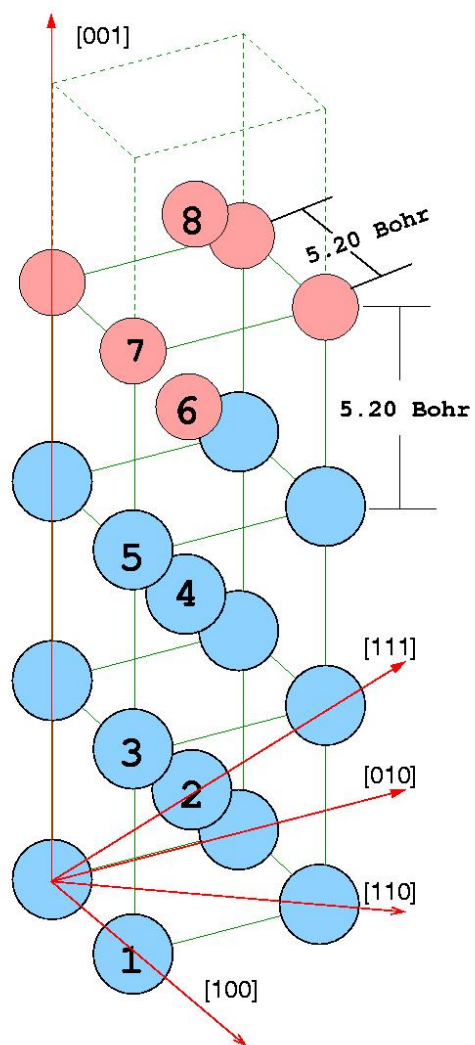


Figure 4.1: Position of the eight atoms in the supercell stacked along  $[001]$  axis. The in-plane and out-of-plane lattice constant is 5.20 Bohr ( $2.71 \text{ \AA}$ ). Also shown are the different crystal lattice directions.

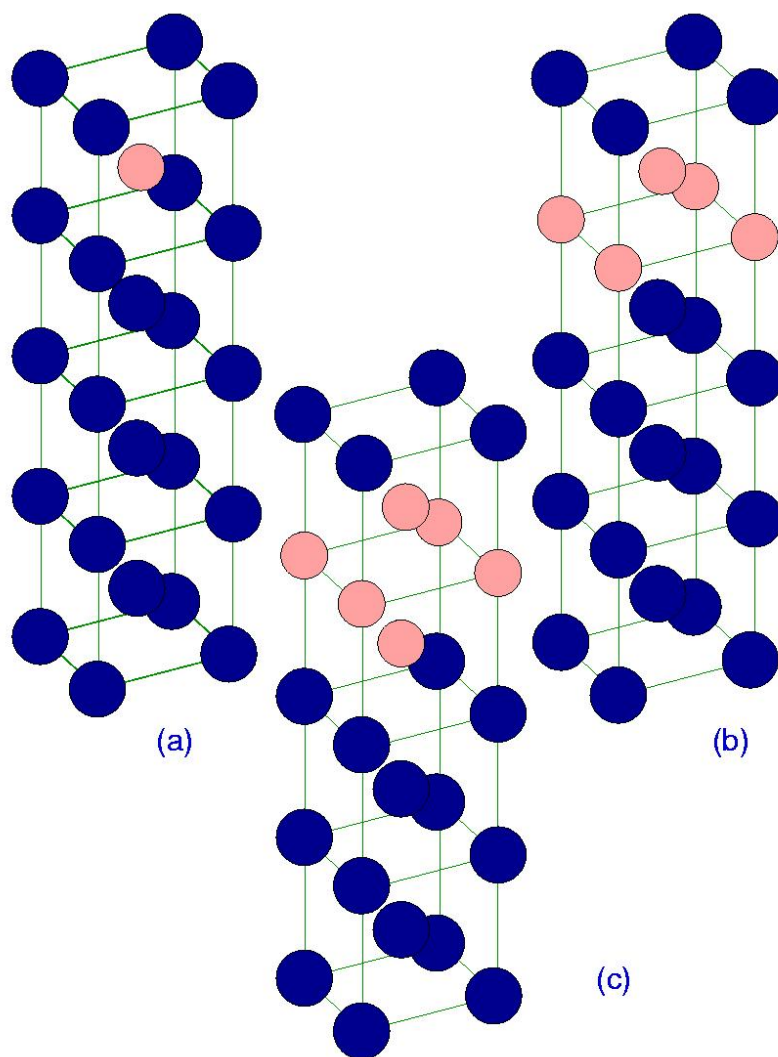


Figure 4.2: Geometry of the supercells: (a)  $\text{Fe}_7/\text{Co}_1$ , (b)  $\text{Fe}_6/\text{Co}_2$  and (c)  $\text{Fe}_5/\text{Co}_3$ . Dark-colored spheres are Fe atoms and the light-colored ones are Co atoms.

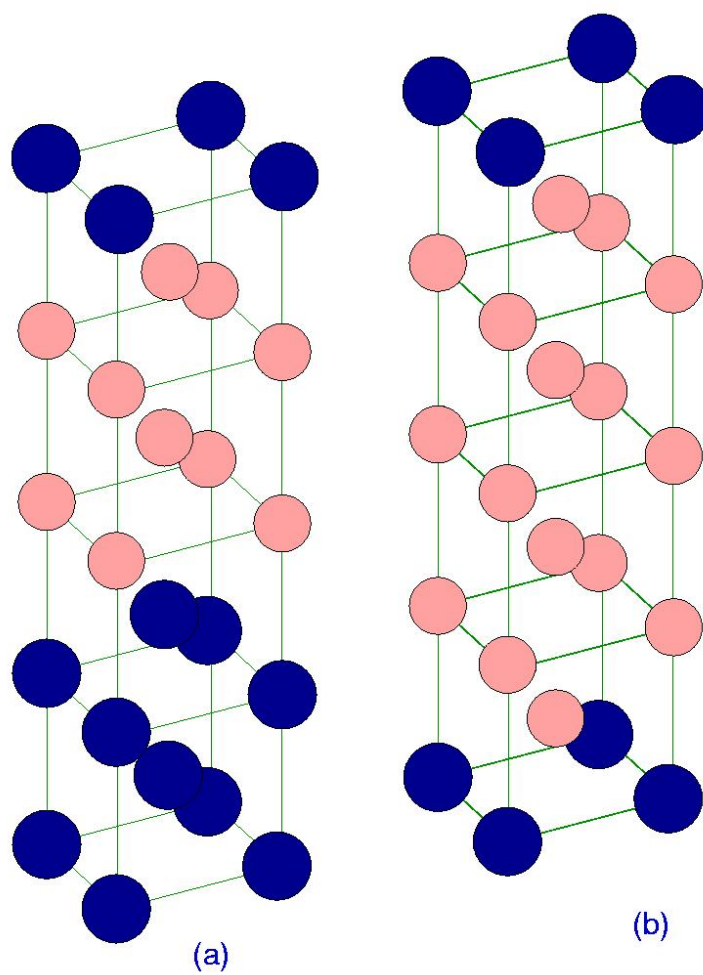


Figure 4.3: Geometry of other supercells: Dark-colored spheres are Fe atoms and the light-colored ones are Co atoms. (a)  $\text{Fe}_4/\text{Co}_4$  and (b)  $\text{Fe}_1/\text{Co}_7$ .

calculated total energy, first for bulk Fe, as a function of the number of  $k$  points. The total energies are compared with the most accurate data, i. e., the value of energy calculated at highest BZ density (810  $k$  points),  $E_o$ . We notice that we need at least 150  $k$  points in the irreducible part of the BZ in order to have a well converged total energy of the system. All total energy calculations were done with sufficiently large number of  $k$  points based on this convergence test to ensure that the sampling of the BZ was well converged.

Another parameter that needs to be chosen carefully is the set of  $\kappa$ , which is related to the kinetic energy of the atoms in the three dimensional lattice. The lattice parameter was initially fixed to a value that is large enough for the chosen atom(s). The multiple  $\kappa$  set obtained for bulk Fe configuration are -0.5, 0.6 and 2.2 corresponding to the x, y and z directions. The same procedure was done in obtaining 1.3, 2.2 and 0.9 for bulk bcc Co.

Energy minimization method obtained an equilibrium MT radius of 2.2 Bohr for bulk Fe. In Figure 4.5, we see that the energy is minimum at a lattice volume of 140.6 Bohr<sup>3</sup> (20 Å<sup>3</sup>). The given energy values are normalized to the minimum energy,  $E_{min}$ , in the magnetic state of the bulk material. To verify the magnetic nature of bulk Fe, calculations were also made for Fe with a nonmagnetic state at the equilibrium volume. A relative total energy difference of 15.74 mRy is observed with a higher total energy in the nonmagnetic case. This verifies that bulk iron prefers a magnetic

state and the calculated magnetic moment per atom is  $2.05 \mu_B$ , which is comparable to the expected value of  $2.2 \mu_B$  [5].

For a hypothetical bcc Co in bulk, the volume at which it will be energetically stable is determined to be  $138.2 \text{ Bohr}^3$  ( $19.6 \text{ \AA}^3$ ). Calculation of this value was obtained for a muffin-tin radius of  $2.1 \text{ Bohr}$ . A slightly smaller muffin-tin radius is expected for Co compared to that of Fe since the latter has a bigger atomic radius. We note in Figure 4.6 a difference of  $18.48 \text{ mRy}$  in the total energy between the nonmagnetic and magnetic state. A higher total energy is expected in the nonmagnetic state. We can tell from this graph that when in a bcc structure, bulk Co prefers a magnetic ground state since taking it to be nonmagnetic gives a higher total energy value. The calculated magnetic moment per atom is  $1.72 \mu_B$ . This value is very close to the accepted value of magnetic moment of Co in hcp structure and Co in fcc structure, which are  $1.72 \mu_B$  and  $1.75 \mu_B$ , respectively [49]. The results of calculations for bulk Fe and Co are summarized in Table 4.1 together with the obtained values for MAE for different spins directed at  $[001]$ ,  $[100]$ ,  $[110]$  and  $[101]$  axes. The numerical calculations were able to reproduce the in-plane easy axis along  $[100]$  for bulk iron [32] whereas an easy axis along  $[001]$  is predicted for bcc cobalt. The MAE values are found to be higher for Fe than for Co.

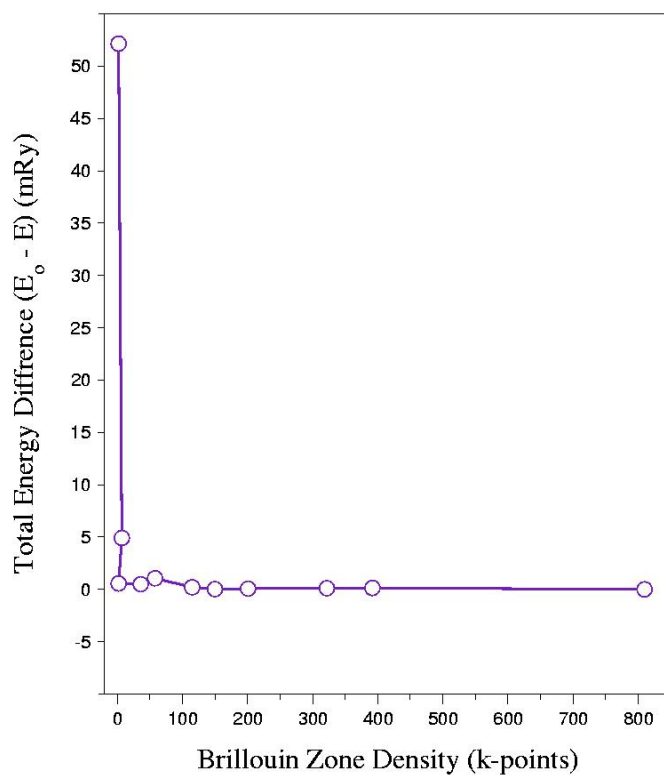


Figure 4.4: Changes in total energy of Fe bulk as a function of the total number of  $k$  points in the whole Brillouin zone.  $E_o$  is the most accurate energy computed with higher BZ density.

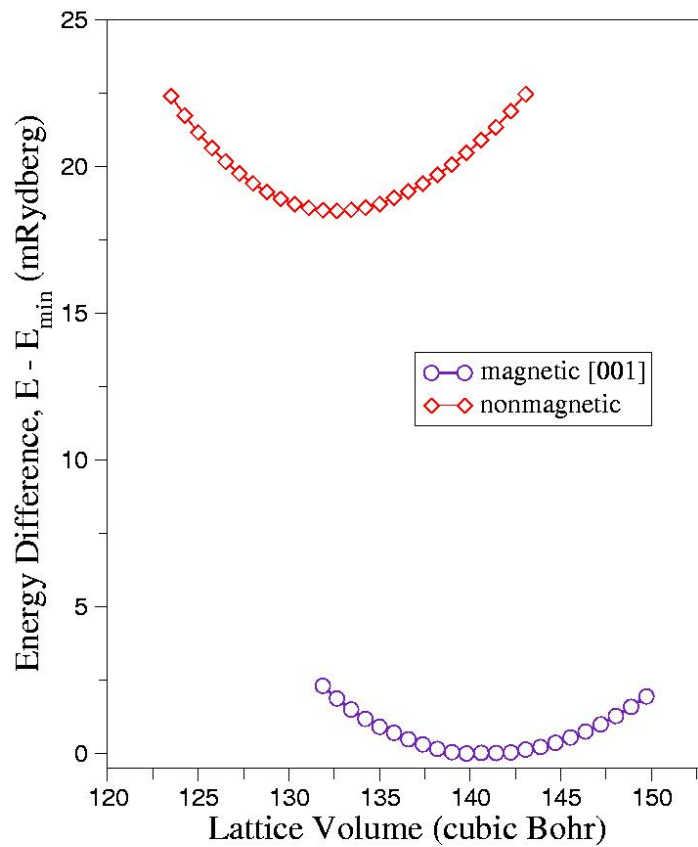


Figure 4.5: Bulk bcc iron. This shows the ground state energy and volume of magnetic bulk iron. Total energy differences are normalized with respect to the lowest energy,  $E_{min}$ , obtained in magnetic Fe.

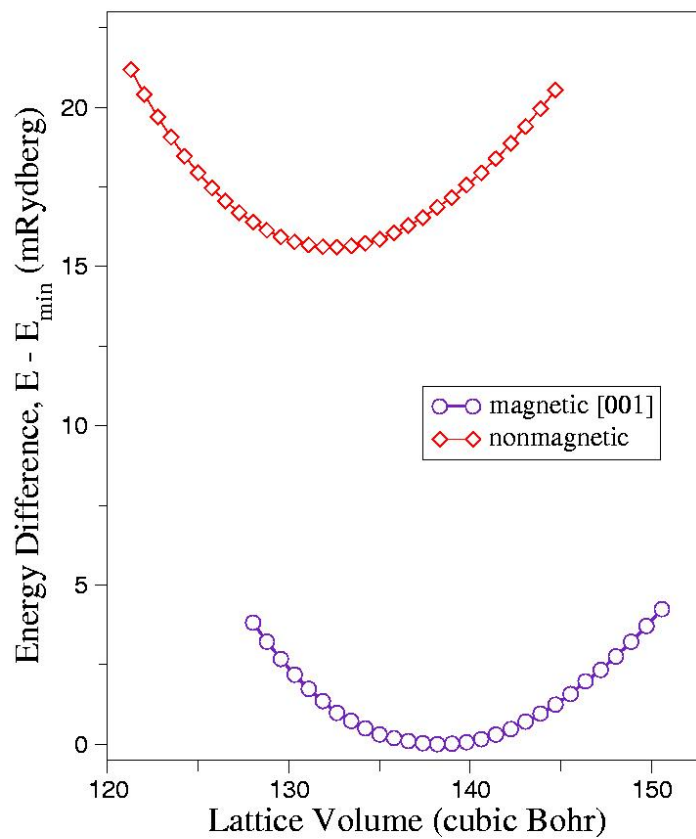


Figure 4.6: Bulk bcc cobalt. This shows ground state energy and lattice volume of hypothetical magnetic bulk bcc cobalt. Total energy differences are normalized with respect to the lowest energy,  $E_{min}$ , obtained in magnetic Co.

Table 4.1: FPLMTO calculations of the magnetic moment per atom and magnetic anisotropy energy per atom of bcc Fe and bcc Co in bulk.

bulk material	bcc Fe	bcc Co
magnetic moment ( $\mu_B$ )	2.05 [100]	1.72 [001]
MAE/vol (mRy/Bohr <sup>3</sup> )	8.89x10 <sup>-7</sup> [001]	7.06x10 <sup>-12</sup> [100]
MAE/vol (mRy/Bohr <sup>3</sup> )	1.33x10 <sup>-8</sup> [110]	9.77x10 <sup>-12</sup> [110]
MAE/vol (mRy/Bohr <sup>3</sup> )	4.27x10 <sup>-6</sup> [101]	4.61x10 <sup>-12</sup> [101]

## 4.2 Fe/Co Multilayers

In all the multilayer systems considered, Co atoms are stacked on top of Fe atoms and thus the atoms being referred to as layer 1 are Fe atoms. The ones deposited on top of the first layer are layer 2 atoms and so on. In addition, atoms consisting the supercells form a bcc structure when repeated in space. The Co atoms are made to occupy bcc lattice points on top of Fe atoms and thus, acquire a bcc structure except for the Co in supercell Fe<sub>7</sub>/Co<sub>1</sub> (refer to Figure 4.2). Here, Co takes on a simple cubic structure when the supercell is repeated in space. Co layers in each supercell were made only a few monolayers thick and are always thinner than Fe layers. A bcc Co in Fe/Co superlattice can be grown on MgO (001) when the thickness of the Co layer is less than 25 Å [8]. Fe<sub>1</sub>/Co<sub>7</sub> was used to represent a system that is richer in Co. With this configuration, the converged equilibrium lattice parameters obtained for bulk Fe were used for multilayer calculations. The effect of changes in volume from Fe to Co lattice volume on the magnetization of the multilayers is discussed in Appendix A.

### 4.2.1 Equilibrium Energy

The total energies of the individual atoms in the superlattice were compared to the corresponding type of atoms in bulk. As the superlattice becomes richer in Co, the total energy of bulk Fe changes due to the reduction in the number of the same type of atoms in its neighborhood. To calculate for the energy difference, the energy of a single Fe (Co) atom is subtracted from the calculated superlattice energy for every Co (Fe) that is added to the system then compared it with that of the pure Fe (Co). Table 4.2 shows the difference in equilibrium energy per atom of multilayers with respect to the total energy of the material indicated in square brackets. The highest change in energy with respect to the pure cases occurred for the multilayer with greatest Co concentration while minimal changes in energy were obtained for 25% Co concentration. Intermediate changes in energy were obtained for Fe-rich superlattices and that with 50% concentration. Note that only in the case where Co concentration is  $\sim 13\%$  that the energy decreased. Addition of several Co atoms to the supercell causes an increase in the total energy making the system of higher Co concentration less stable. This is due to the lattice mismatch between Fe and Co and that Co atoms prefer to be in an hcp state than in a bcc structure.

Table 4.2: Difference in equilibrium energy per atom of multilayers with respect to bulk Fe and Co.

Multilayer	Energy difference (mRy) [bcc Fe]	Energy difference (mRy) [ bcc Co]
Fe <sub>7</sub> /Co <sub>1</sub>	-0.611	-0.536
Fe <sub>6</sub> /Co <sub>2</sub>	0.210	0.285
Fe <sub>5</sub> /Co <sub>3</sub>	0.286	0.361
Fe <sub>4</sub> /Co <sub>4</sub>	0.417	0.492
Fe <sub>1</sub> /Co <sub>7</sub>	0.868	0.944

## 4.2.2 Magnetocrystalline Anisotropy

The total energy of the multilayers were calculated with the magnetic moment oriented at different directions. From the obtained easy axis of bulk Fe at [100] axis, there is a transition of the easy axis to [110] direction as the multilayer becomes richer in Co. All the multilayers considered are found to have easy axis along the [110] direction. This result is similar to the experimental findings of the team of Hagstrom [35], who observed that the magnetic moments of Fe/Co (001) multilayers have no perpendicular component with respect to the sample plane. The results of the MAE calculations are tabulated in Table 4.3. The MAE involved in out-of-plane rotations are higher compared to that of in-plane spin rotations. The decrease in the number of similar type of atoms in the "line of sight" when rotating spins out-of-plane contribute to this behavior.

In Figure 4.7, we show the calculated out-of-plane anisotropy energy of the multilayers for different Co concentration. The plot shows that the MAE increases for

increasing Co concentration.  $\text{Fe}_4/\text{Co}_4$  has the greatest anisotropic energy when changing the magnetic direction from [110] to [001].

Table 4.3: FPLMTO calculations of the magnetic moment per atom and magnetic anisotropy energy per atom of  $\text{Fe}_7/\text{Co}_1$ ,  $\text{Fe}_6/\text{Co}_2$ ,  $\text{Fe}_5/\text{Co}_3$ ,  $\text{Fe}_4/\text{Co}_4$  and  $\text{Fe}_1\text{Co}_7$ . The total energies were calculated for superlattice spin at [001], [100] and [110] axes. Note that the easy axis of all the multilayers is the [110] direction.

Multilayers	MAE/vol (mRy/Bohr <sup>3</sup> ) [001]	MAE/vol (mRy/Bohr <sup>3</sup> ) [100]
$\text{Fe}_7/\text{Co}_1$	$2.22 \times 10^{-5}$	$8.89 \times 10^{-7}$
$\text{Fe}_5/\text{Co}_3$	$1.85 \times 10^{-4}$	$1.17 \times 10^{-7}$
$\text{Fe}_6/\text{Co}_2$	$2.85 \times 10^{-5}$	$3.56 \times 10^{-7}$
$\text{Fe}_4/\text{Co}_4$	$2.35 \times 10^{-4}$	$8.89 \times 10^{-7}$
$\text{Fe}_1/\text{Co}_7$	$1.25 \times 10^{-4}$	$8.90 \times 10^{-7}$

### 4.2.3 Magnetization

Next we report on the calculated spin moments of the atoms in Fe/Co multilayers. Figure 4.8 shows the average magnetic moment per atom for different Co concentrations. Values for average spin moment decreases for increasing Co content. However, there is a slight upturn in the value of magnetic moment when the Co concentration is 50%. This behavior of decreasing average moment is comparable to the theoretical work of Eriksson, et al [41].

In Figure 4.9, The magnetic moments of atoms located at the interface are plotted for increasing Co content. At the interface, a significant enhancement in the magnetic

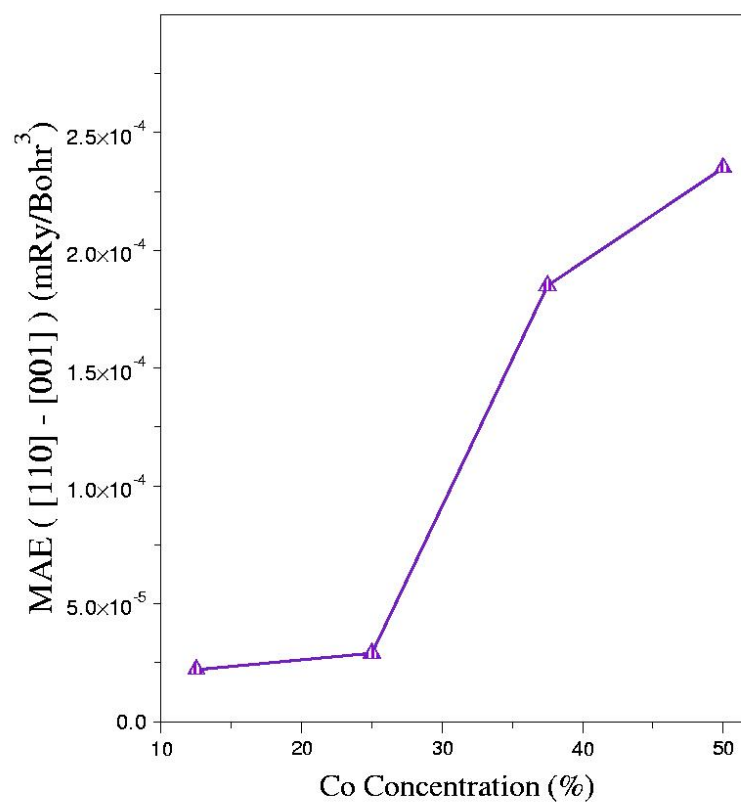


Figure 4.7: Calculated MAE per volume as a function of Co concentration.

moment of Fe is obtained. The magnetic moment increased about 17–24% compared to pure Fe bulk moment. Magnetic moments of Fe are enhanced, becoming as large as  $2.5 \mu_B$ , if the concentration of neighboring Co atoms is high.

This is not the case for Co atoms located at the interface as they did not show any significant change in the magnetic moment compared to its bulk value. The Co interface moments are similar to that for bulk environment, changing only about 0.8 – 3%. These results can be compared to theoretical [39] and experimental [6] works that show an enhancement in magnetic moment of Fe at the interface whereas the Co moment is constant.

We compare this behavior with that of the magnetic moments of the atoms located at the embedded layers. Values for the spin moment of the atoms immediately next to the interface layer as a function of Co concentration is plotted in Figure 4.10 and are found to be weaker than those at the interface. As seen in the figure, the magnetic moments of the atoms in the central layers are weaker than those at the interface. In fact, the values are very nearly similar to the bulk Fe moment with differences only ranging from  $\sim 3 - 4\%$ . Magnetic moments of atoms, in this case, are still similar with its corresponding moment in the bulk.

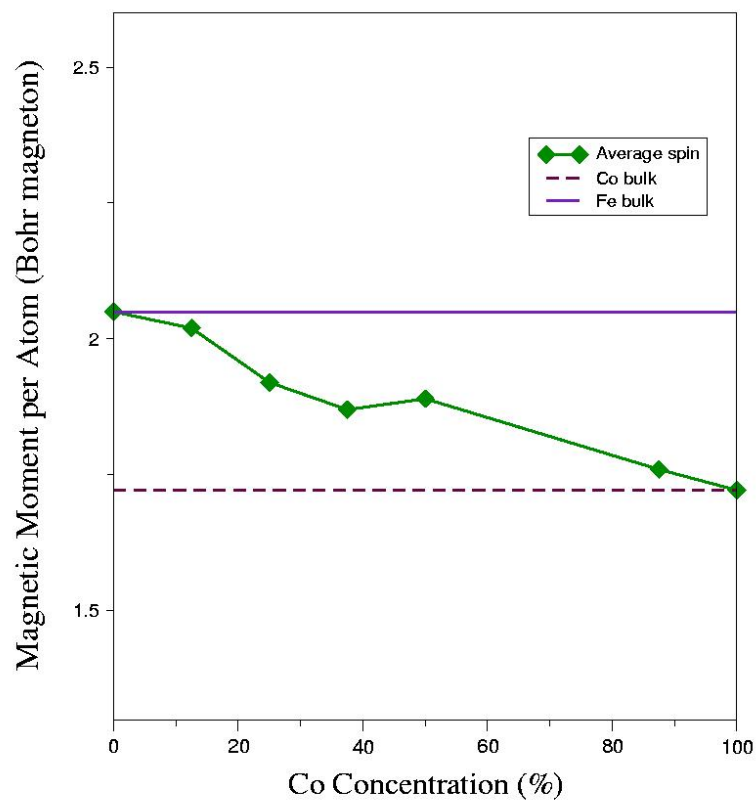


Figure 4.8: Calculated average spin moments of Fe/Co multilayers,  $\text{Fe}_7/\text{Co}_1$ ,  $\text{Fe}_6/\text{Co}_2$ ,  $\text{Fe}_5/\text{Co}_3$ ,  $\text{Fe}_4/\text{Co}_4$ ,  $\text{Fe}_1/\text{Co}_7$  for different Co concentrations. Solid line represents Fe bulk moment and dashed line marks the Co bulk moment.

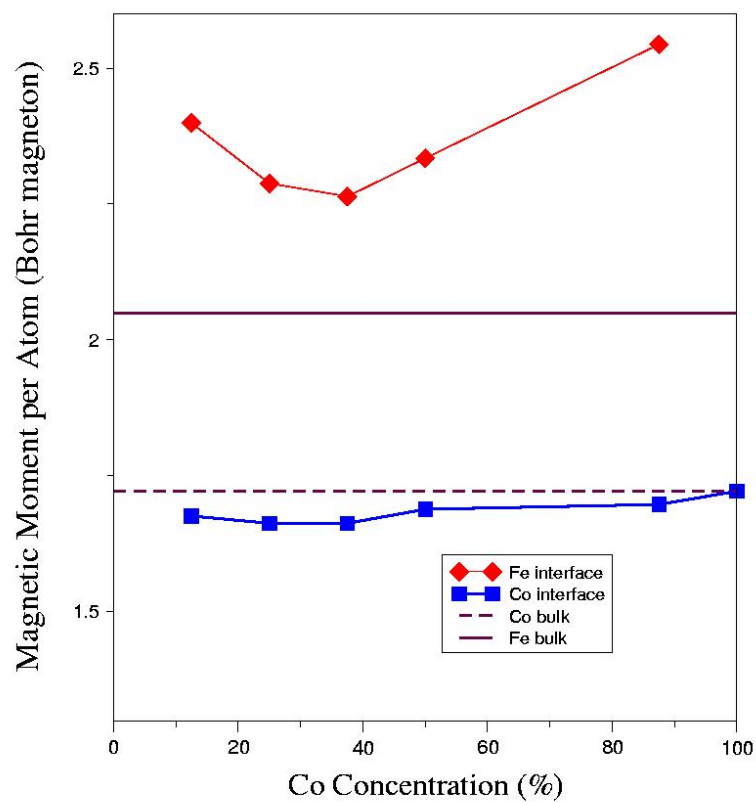


Figure 4.9: Calculated spin moments of atom at the interface of Fe/Co multilayers,  $\text{Fe}_7/\text{Co}_1$ ,  $\text{Fe}_6/\text{Co}_2$ ,  $\text{Fe}_5/\text{Co}_3$ ,  $\text{Fe}_4/\text{Co}_4$ ,  $\text{Fe}_1/\text{Co}_7$  for increasing Co concentrations. Solid line represents Fe bulk moment and dashed line marks the Co bulk moment.

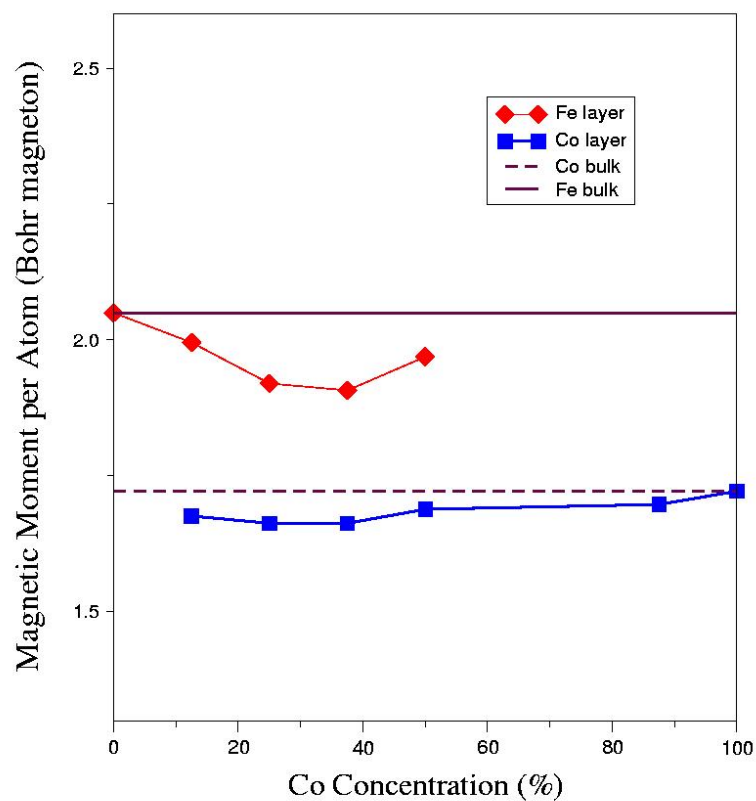


Figure 4.10: Calculated spin moment of atoms close to the interface of Fe/Co multilayers,  $\text{Fe}_7/\text{Co}_1$ ,  $\text{Fe}_6/\text{Co}_2$ ,  $\text{Fe}_5/\text{Co}_3$ ,  $\text{Fe}_4/\text{Co}_4$ ,  $\text{Fe}_1\text{Co}_7$  for different Co concentrations. Solid line represents Fe bulk moment and dashed line marks the Co bulk moment.

Table 4.4: Difference in equilibrium energy per atom of Fe<sub>6</sub>/Co<sub>2</sub> multilayer with intermixed Fe and Co layer compared to bulk Fe and Co and Case 1.

Multilayer	$\Delta E$ (mRy) [bcc Fe]	$\Delta E$ (mRy) [bcc Co]	$\Delta E$ (mRy) [Case 1]
Case 2	0.591	0.667	0.381
Case 3	1.129	1.204	0.919

#### 4.2.4 Intermixing

In experimentally fabricated Fe/Co multilayers, x-ray diffraction measurements show 1 up to 2 monolayers of intermixing between Fe and Co atoms during deposition [6]. The atoms in the supercell containing 25% Co concentration then were rearranged such that the Co atoms are at least one monolayer thickness apart to simulate imperfect interfaces. Diagrams of the two different supercells (Cases 2 and 3) having the same Co content with Case 1 are shown in Figure 4.11. Case 1 has two Co layers adjacent to one another at layers 7 and 8. For cases 2 and 3, Co layers are located at layers 5 and 8, and layers 6 and 8, respectively. Tabulated total energy difference of individual atoms of the two cases compared to pure materials and the configuration of Case 1 is shown in Table 4.4. The configuration in case 2 has a smaller energy change per atom from the bulk energy compared to that of case 3. Note that the latter is the superlattice that contain alternating single monolayers of Fe and Co. A lower energy is obtained for multilayers having thicker Fe layers intermixed with relatively thinner Co layers, hence, more stable.

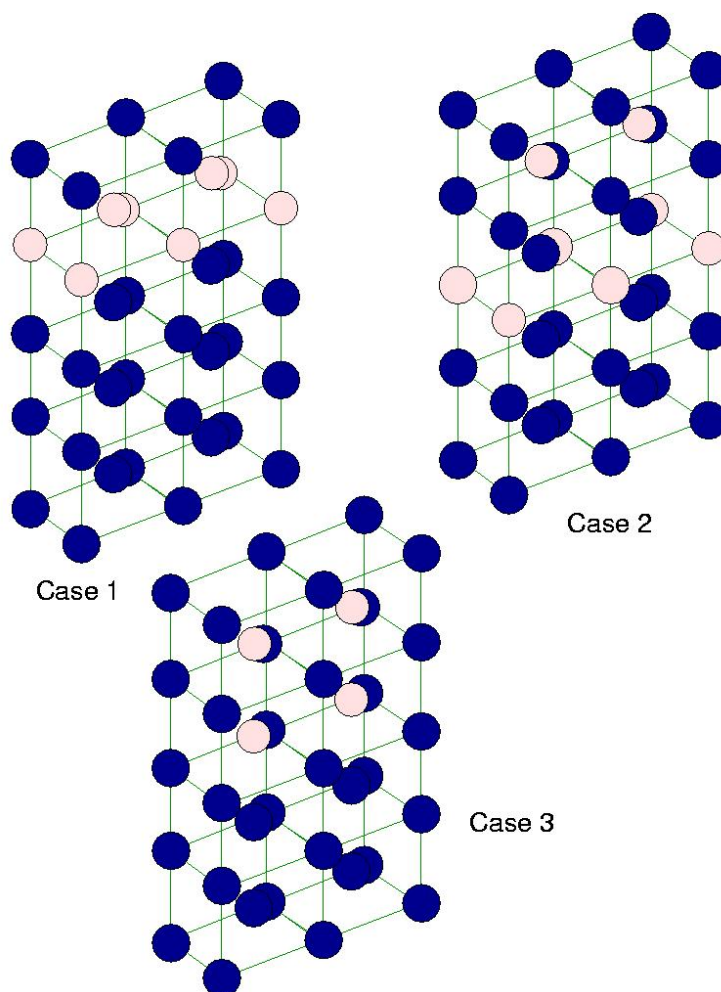


Figure 4.11: Fe<sub>6</sub>/Co<sub>2</sub> multilayers. The layers composed of Co atoms are intermixed with Fe layers. Case 1: adjacent Co atoms; Case 2: 2 monolayers of Fe separate the 2 Co layers. Case 3: 1 monolayer thickness apart.

Magnetic profiles of the three configurations of  $\text{Fe}_6/\text{Co}_2$  are shown in Figure 4.12. Two tendencies can be distinguished from this figure; the average magnetic moment per atom increases from case 1 to case 3 and that for the same concentration of Fe and Co atoms, the arrangement of atoms in the superlattice affects the magnetic moment of the Fe atoms at the interface. The highest average moment is obtained for Case 2 configuration.

To better visualize this phenomenon, Figure 4.13 show the intermixed portions of the multilayers in Cases 1 and 2. When a single monolayer of Fe is placed in between two Co layers, as in (a), the sandwiched Fe magnetic moment is greatly increased as high as 27% compared to that of the Fe atoms having Co and another Fe at its top and bottom layers.

Farther from the interface, on the other hand, Fe atoms maintain the magnetic moment value as in bulk Fe. In the case of Co, atoms at the interface and those located farther from the interface have the same magnetic moment as the bulk Co. While moments of Fe atoms at the interface are greatly enhanced, moments Co atoms in all of the configurations remain unchanged. These enhancements of the Fe magnetic moment is an evidence of the redistribution of the charge density in the solid whenever Fe is surrounded by a different magnetic atom. However, specific details of this redistribution can be investigated through the multilayers' density of states, the calculation of which is beyond the scope of this present study.

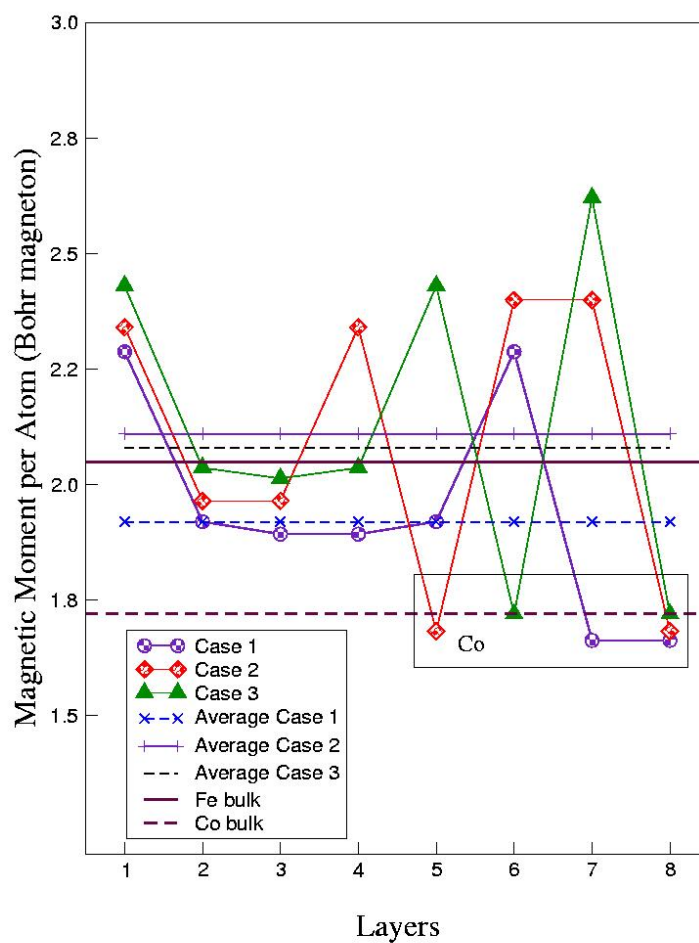


Figure 4.12: Calculated magnetic moment of atoms in the Fe<sub>6</sub>/Co<sub>2</sub> multilayer for the 3 different cases. Solid line represents Fe bulk moment and dashed line marks the Co bulk moment. Region inside the box contain magnetic moments of Co atoms and the remaining in the graph are magnetic moments of Fe atoms.

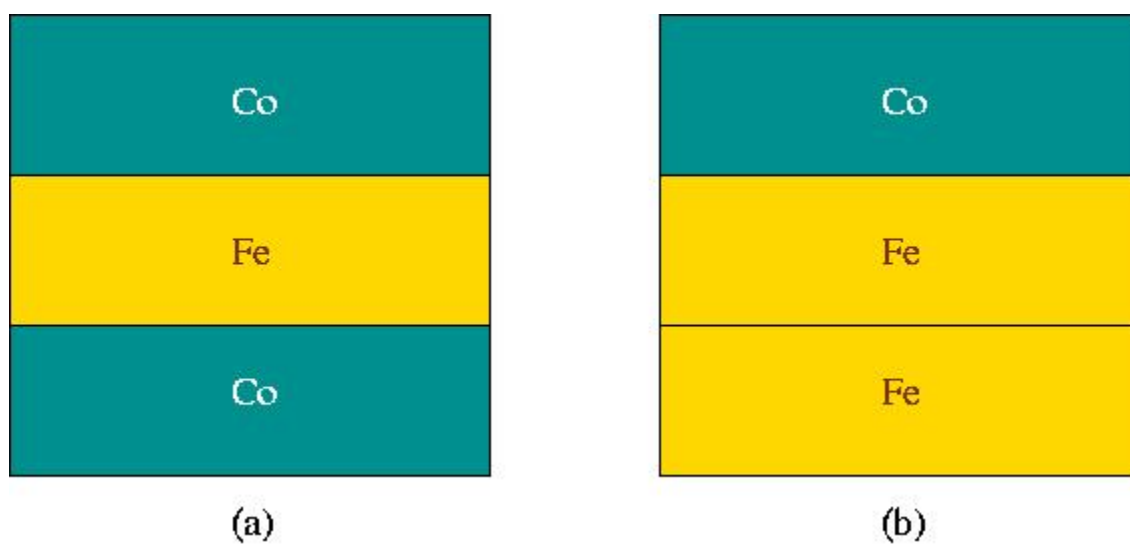


Figure 4.13: Intermixed portions of  $\text{Fe}_6/\text{Co}_2$  multilayer in Cases 2 and 3 configurations. The increase in magnetic moment of the sandwiched Fe layer in (a) is 27% while in (b) is 17% compared to the bulk Fe moment.

# Chapter 5

## Summary and Conclusions

The magnetization and anisotropy of Fe/Co (001) multilayers have been calculated from first-principles by means of self-consistent FP-LMTO method based on density functional theory. We have verified the equilibrium parameters for bulk bcc Fe and bcc Co. Energy calculations for the Fe/Co superlattices show that energy stabilizes when bcc Co is only a few monolayers thick. The magnetization was investigated for varying concentrations of constituent atoms. Average magnetic moment per atom decreases with increasing Co concentration. We have shown from the magnetic profiles of the multilayers that the Fe atom located at the interface is found to have significantly enhanced magnetic moment compared to that of the Fe atoms farther from the interface. The greatest increase in Fe moment is obtained for the multilayer with highest Co concentration. Co atoms at the interface, on the other hand, behave

similarly to Co atoms in the bulk environment.

For multilayers with the same concentration, location of atoms in the multilayers affect the magnetic properties. Fe atoms that are sandwiched between two Co atoms show even larger increase in magnetic moment than when placed adjacent to another Fe layer and Co. No significant changes in Co moment was observed even when the number of neighboring Fe and Co atoms changes.

The magnetocrystalline anisotropy energies were successfully resolved using total energy approach. Bulk Fe has an easy axis along  $[100]$  plane while the easy axis for hypothetical bcc Co is along  $[001]$  direction. All the multilayer systems considered have easy axis along  $[110]$  plane. In-plane anisotropic energies become higher for increasing Co content.

Magnetization and MAE of magnetic materials are greatly affected by its atomic environment. Hence, it is necessary to find optimal parameters and multilayer conditions. In addition, a hypothetical material can be made to stabilize and exhibit desirable properties of materials that cannot be achieved in naturally existing bulk form. The bcc Fe/Co has been successfully synthesized and it has been known to exhibit desirable magnetic properties. The results of present theoretical work verifies this.

A detailed theoretical understanding of the magnetic properties of a potential multilayer system is important so that we can have a full map of the materials'

preferred structure even before it is actually synthesized. It is now possible to tailor such materials down to the finest details of electronic structure that will yield unique structures with enhanced functionality.

# Appendix A

## Magnetovolume Sensitivity of Fe and Co Multilayers

From the calculations, bulk bcc Fe and Co have a lattice mismatch of 0.6% with Fe being less compact. The choice of lattice parameters in all multilayers obtained from bulk calculations was qualified through energy minimization, i. e., more energetically stable configuration is given preference. The graph in Figure A.1 illustrates this simple test. Magnetization of bulk bcc Co is shown to stabilize at a lattice volume of 148.8 Bohr<sup>3</sup> (21 Å<sup>3</sup>) having a value of 1.68  $\mu_B$ . At this volume, the magnetic moment of Fe is 2.15  $\mu_B$ . The plot extends up to 151.4 Bohr<sup>3</sup> (21.5 Å<sup>3</sup>) and the same value for the magnetization of Fe is obtained. Difference in equilibrium lattice volumes with that having maximum magnetic moment is 2.5% for both Fe and Co atoms.

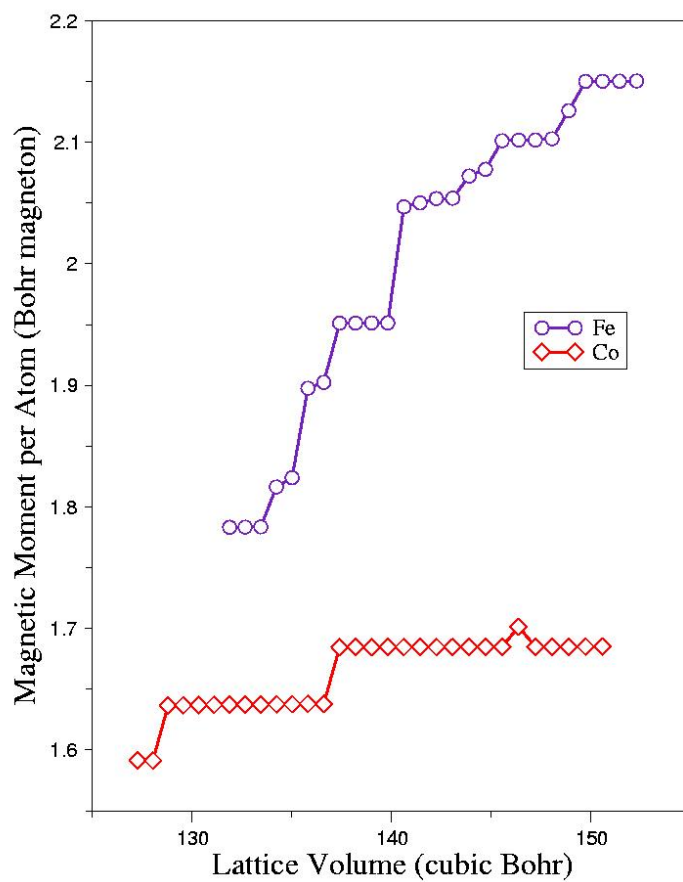


Figure A.1: Magnetic moment of bulk bcc Fe and bcc Co as a function of lattice volume.

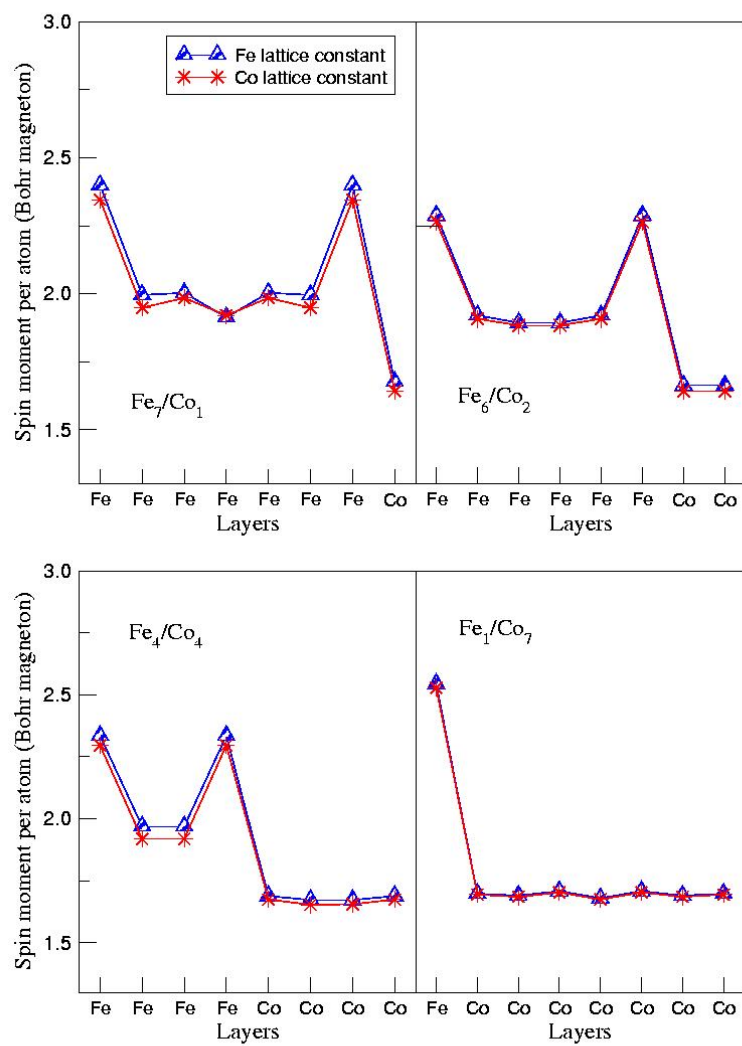


Figure A.2: Layer by layer magnetic moment of Fe/Co multilayers calculated using Fe and Co lattice constants .

The same test was performed for Fe/Co multilayers. We look into the changes in magnetic moment of the system for two different lattice constants. This verifies the advantage in Figure A.2, no significant volume effects are observed except for lower spin moments of Fe atoms located next to the interface layer of superlattices with 12% and 50% concentration of Co. Magnetic moments of Co, on the other hand, show no drastic changes for the two lattice constants. Differences with the spin moment for every atom ranges from 2.9 – 3.2%.

Deviations between the magnetic profiles for these two lattice volumes give information on the relaxation effects of on the magnetization. In the case of bcc Fe/Co (001), the magnetic moment of the atoms have no dramatic volume dependence.

# Bibliography

- [1] N. Argaman and G. Makov. Thermodynamics as an alternative foundation for zero-temperature density-functional theory and spin-density functional theory. *Phys. Rev. B*, 66:052413–1–4, 2002.
- [2] O. Le Bacq, O. Eriksson, B. Johansson, P. James, and A. Delin. First-principles calculations of the magnetic anisotropy energy of Fe-V multilayers. *Phys. Rev. B*, 65:134430–1–9, 2002.
- [3] M.N. Baibich, J.M. Broto, A. Fert, F. Nguyen van Dau, F. Petroff, P. Etienne, G. Creuzet, A. Friedrichs, and J. Chazelas. Giant magnetoresistance of (001)Fe/(001)Cr magnetic superlattice. *Phys. Rev. Lett.*, 61:2472–2475, 1988.
- [4] G. Binasch, P. Grunberg, F. Saurenbach, and W. Zinn. Enhanced magnetoresistance in layered magnetic structures with antiferromagnetic interlayer exchange. *Phys. Rev. B*, 39:4828–4820, 1989.

- [5] P. Blomqvist. *Structural and Magnetic Properties of Fe/Co (001) and Fe/V (001) Superlattices*. PhD thesis, Uppsala University, 2001.
- [6] P. Blomqvist, R. Wäppling, A. Broddefalk, P. Nordblad, S. G. E. te Velthuis, and G. P. Felcher. Structural and magnetic properties of bcc Fe/Co(001) superlattices. *J. Magn. Magn. Mater.*, 248:75–84, 2002.
- [7] S. Blundell. *Magnetism in Condensed Matter*, chapter 6. Oxford University Press, Inc., 2001.
- [8] A. Broddefalk. *Magnetic Properties of transition metal compounds and superlattices*. PhD thesis, Uppsala University, 2000.
- [9] A. Broddefalk, R. Mathieu, P. Nordblad, P. Blomqvist, R. Wäppling, J. Lu, and E. Olsson. Interlayer exchange coupling and giant magnetoresistance in Fe/V (001) superlattices. *Phys. Rev. B*, 65:214430–1–6, 2002.
- [10] P. Bruno. Theory of interlayer magnetic coupling. *Phys. Rev. B*, 52:411–439, 1995.
- [11] A. Chaiken, R. P. Michel, and M. A. Wall. Structure and magnetism of Fe/Si multilayers grown by ion-beam sputtering. *Phys. Rev. B*, 53:5518–5529, 1996.
- [12] M. Cinal, D. M. Edwards, and J. Mathon. Magnetocrystalline anisotropy in ferromagnetic films. *Phys. Rev. B*, 50:3754, 1994.

- [13] S. Colis, A. Dinia, C. Mny, P. Panissod, C. Ulhaq-Bouillet, and G. Schmerber. Magnetic, transport, and structural properties of Fe/Co/Cu/[Co/Ir/Co] sandwiches and Fe/Co/Cu/[Co/Ir] multilayers prepared by ion-beam sputtering. *Phys. Rev. B*, 62:11709–11718, 2000.
- [14] G. H. O. Daalderop, P. J. Kelly, and F. J. A. den Broeder. Prediction and confirmation of perpendicular magnetic anisotropy in Co/Ni multilayers. *Phys. Rev. Lett.*, 68:682–685, 1992.
- [15] G. H. O. Daalderop, P. J. Kelly, and M. F. H. Schuurmans. First-principles calculations of the magnetic anisotropy of  $(Co)_n/(X)_m$  multilayers. *Phys. Rev. B*, 42, 1990.
- [16] G. H. O. Daalderop, P. J. Kelly, and M. F. H. Schuurmans. Magnetic anisotropy of free-standing Co monolayer and of multilayers which contain Co monolayers. *Phys. Rev. B*, 50:9989–10003, 1994.
- [17] B. Dieny, S. Speriou, S. S. P. Parkin, B. A. Gurney, D. R. Wilhoit, and D. Mauri. Giant magnetoresistance in soft ferromagnetic multilayers. *Phys. Rev. B*, 43:1297–1300, 1991.
- [18] L. Doü, R. Bertacco, G. Isella, F. Ciccacci, and M. Richter. Electronic and magnetic properties of the Co/Fe(001) interface and the role of oxygen. *Phys. Rev. B*, 61:15 294–15 301, 2000.

- [19] J. M. DuMond and J. P. Youtz. Selective X-Ray Diffraction from Artificially Stratified Metal Films Deposited by Evaporation. *Phys. Rev.*, 48:703–709, 1935.
- [20] J. M. Gallego, D. Lederman, S. Kim, and I. K. Schuller. Oscillatory Behavior of the Transport Properties in Ni/Co Multilayers: A Superlattice Effect. *Phys. Rev. Lett.*, 74:4515–4518, 1995.
- [21] P. Grünberg. Layered magnetic structures: History, highlights, applications. *Physics Today*, 54:31–37, May 2001.
- [22] P. Grünberg, R. Schreiber, Y. Pang, M. B. Brodsky, and H. Sowers. Layered magnetic structures: Evidences for Antiferromagnetic Coupling in Fe Layers Across Cr Interlayers. *Phys. Rev. B*, 57:2442, 1996.
- [23] O. Gunnarsson and B. I. Lundqvist. Exchange and correlation in atoms, molecules and solids by the spin-density functional formalism. *Phys. Rev. B*, 13:4274–4299, 1976.
- [24] R. Gupta, M. Weisheit, H.-U. Krebs, and P. Schaaf. Interface structure of Fe/Ag multilayers prepared by pulsed laser deposition. *Phys. Rev. B*, 67:075402–1–3, 2003.
- [25] E. M. Gyorgy, D. B. McWhan, J. F. Dillon, L. R. Walker, and J. V. Waszczak. Magnetic behavior and structure of compositionally modulated Cu-Ni thin films. *Phys. Rev. B*, 25:6739–6747, 1982.

- [26] H. W. Hugosson. *Theoretical studies of phase stabilities and electronic structure in molybdenum carbide*. PhD thesis, Uppsala University, 1999.
- [27] Y. Huttel, J. Avila, M.C. Asensio, P. Bencok, C. Richter, V. Ilakovac, O. Heckmann, and K. Hricovini. Auger electron diffraction study of V/Fe (100) interface formation. *Surf. Sci.*, 402-404:609–613, 1998.
- [28] I. K. Schuller and S. Kim and C. Leighton. Magnetic Superlattices and Anisotropy. *J. Magn. Magn. Mater.*, 200:571–582, 1999.
- [29] Y. U. Idzerda, W. T. Elam, B. T. Jonker, and G. A. Prinz. Structure determination of metastable cobalt films. *Phys. Rev. Lett.*, 62:2480–2483, 1989.
- [30] J. d’Albuquerque e Castro and M. S. Ferreira and R. B. Muniz. Theory of the exchange coupling in magnetic metallic multilayers. *Phys. Rev. B*, 49:16062–16065, 1994.
- [31] R.O Jones and O. Gunnarson. The density functional formalism, its applications and prospects. *Rev. Mod. Phys.*, 61:689–699, 1989.
- [32] C. Kittel. *Introduction to Solid State Physics*, chapter 15. John Wiley and Sons, Inc., 1996.

- [33] W. Kohn and N. Rostoker. Solution of the Schrödinger Equation in Periodic Lattices with an Application to Metallic Lithium. *Phys. Rev.*, 94:1111–1120, 1954.
- [34] W. Kuch and S. S. P. Parkin. Structural and magnetic phases of Fe in Fe/Ni<sub>81</sub>Fe<sub>19</sub> (001) multilayers. *J. Magn. Magn. Mater.*, 184:127–136, 1998.
- [35] L. Hågström and B. Kalska and E. Nordström and P. Blomqvist and R. Wäppling. Magnetic Anisotropy and Magnetic Fields in bcc Fe/Co (001) Superlattice. *Journal of Alloys and Compounds*, 347:252–258, 2002.
- [36] L. M. Sandratskoo and J. Kübler. Local Magnetic Moments in bcc Co. *Phys. Rev. B*, 47:5854–5860, 1992.
- [37] X. Liu, R. L. Stamps, R. Sooryakumar, and G. A. Prinz. Spin-wave magnetic anisotropies in a thick bcc cobalt film. *Phys. Rev. B*, 54:11 903–11 906, 1996.
- [38] I. K. Marmorkos and S. Das Sarma. Atomistic numerical study of molecular-beam-epitaxial growth kinetics. *Phys. Rev. B*, 45:11262–11272, 1992.
- [39] A. M. N. Niklasson, B. Johansson, and H. L. Skriver. Interface magnetism in 3d transition metals. *Phys. Rev. B*, 61:6373–6382, 1999.

- [40] P. Norblad, A. Broddefalk, and R. Mathieu. Fe/V and Fe/Co (001) superlattices: growth, anisotropy, magnetisation and magnetoresistance. *Physica*, 327:344–349, 2002.
- [41] O. Eriksson and L. Bergqvist and E. Holström and O. LeBacq and S. Frota-Pessoa and B. Hjörvarson and L. Nordström. Magnetism of Fe/V and Fe/Co multilayers. *J. Phys.: Condens. Matter*, 15:S599–S615, 2003.
- [42] S.S.P. Parkin, N. More, and K. P. Roche. Oscillations in Exchange Coupling and Magnetoresistance in Metallic Superlattice Structures: Co/Ru, Co/Cr and Fe/Cr. *Phys. Rev. Lett.*, 64:2304–2308, 1990.
- [43] R. G. Parr and W. Yang. *Density-Functional Theory of Atoms and Molecules*, chapter 3. Oxford University Press, Inc., 1989.
- [44] W. P. Pratt, S. F. Lee, J. M. Slaughter, R. Loloee, P. A. Schroeder, and J. Bass. Perpendicular giant magnetoresistances of Ag/Co multilayers. *Phys. Rev. Lett.*, 66:3060–3063, 1991.
- [45] P. Ravindran, A. Kjekshus, H. Fjellvåg, P. James, L. Nordström, B. Johansson, and O. Eriksson. Large magnetocrystalline anisotropy in bilayer transition metal phases from first-principles full-potential calculations. *Phys. Rev. B*, 63:144409–1–14409–18, 2001.

- [46] C.O. Rodriguez, R. A. Casali, E.L. Peltzer, O.M. Capannini, and M. Methfessel. First-principles pseudopotential and full-potential linear muffin-tin orbital calculation of anharmonic effects on the lattice-dynamical properties of alp. *Phys. Rev. B*, 40:3975–3979, 1989.
- [47] I. K. Schuller. New Class of Layered Materials. *Phys. Rev. Lett.*, 44:1597–1600, 1980.
- [48] J. Shen, P. Ohresser, Ch. V. Mohan, M. Klaua, J. Barthel, and J. Kirschner. Magnetic Moment of fcc Fe(111) Ultrathin Films by Ultrafast Deposition on Cu(111). *Phys. Rev. Lett.*, 80:1980–1983, 1998.
- [49] D. J. Singh. Magnetism in bcc cobalt. *Phys. Rev. B*, 85:2258–2261, 1992.
- [50] M. Springborg. *Methods of Electronic Structure Calculations*, chapter 15. John Wiley and Sons Ltd., 2000.
- [51] P. Srivastava, F. Wilhelm, A. Ney, M. Farle, H. Wende, N. Haack, G. Ceballos, and K. Baberschke. Magnetic moments and Curie temperatures of Ni and Co thin films and coupled trilayers. *Phys. Rev. B*, 58:5701–5706, 1998.
- [52] L. Szunyogh, B. Ujfalussy, and P. Weinberger. Magnetocrystalline anisotropy in ferromagnetic films. *Phys. Rev. B*, 51:9552, 1995.

- [53] B. J. Thaler and J. B. Ketterson. Enhanced Magnetization Density of a Compositionally Modulated CuNi Thin Film. *Phys. Rev. Lett.*, 41:336–339, 1978.
- [54] M. Tischer, O. Hjortstam, D. Arvanitis, J. H. Dunn, F. May, K. Baberschke, J. Trygg, J. M. Wills, B. Johansson, and O. Eriksson. Enhancement of Orbital Magnetism at Surfaces: Co on Cu(100). *Phys. Rev. Lett.*, 75:1602–1605, 1995.
- [55] J. Trygg, B. Johansson, O. Eriksson, and J. M. Wills. Total energy calculations of the magnetocrystalline anisotropy energy in the ferromagnetic 3d metals. *Phys. Rev. Lett.*, 75:2871–2874, 1995.
- [56] L. Turek, V. Drchal, J. Kudrnovsky, M. Sob, and P. Weinberger. *Electronic Structure of Disordered Alloys, Surfaces and Interfaces*, chapter 2. Kluwer, Boston, 1997.
- [57] S. H. Vosko, L. Wilk, and M. Nusair. Accurate spin-dependent electron liquid correlation energies for local spin density calculations: a critical analysis. *Can. J. Phys.*, 58:1200–1211, 1980.
- [58] J. Wills, O. Eriksson, M. Alouani, and D. Price. Full-Potential LMTO Total Energy and Force Calculations. In H. Dreyssé, editor, *Electronic Structure and Physical Properties of Solids*, pages 148–167, Berlin, 2000. Springer-Verlag.
- [59] J. Zabloudil, L. Szunyogh, U. Pustogowa, and P. Weinberger. Magnetic anisotropy of  $\text{Fe}_x \text{Co}_{1-x}$  multilayers on Cu (001): Reorientation transition of

magnetic moments due to different interlayer coupling. *Phys. Rev. B*, 58:6316–6320, 1998.

- [60] L. Zhong, M. Kim, X. Wang, and A.J. Freeman. Overlayer-induced anomalous interface magnetocrystalline anisotropy in ultrathin Co films. *Phys. Rev. B*, 53:9770, 1996.